



Time- and frequency-domain hybridizable discontinuous Galerkin solvers for the calculation of the Cherenkov radiation[☆]

Andrea La Spina^{*}, Jacob Fish

Department of Civil Engineering and Engineering Mechanics, Columbia University, NY, United States of America

Available online xxxx

Abstract

This work proposes novel hybridizable discontinuous Galerkin (HDG) methods, both in the time and in the frequency domain, to accurately compute the Cherenkov radiation emitted by a charged particle travelling in a uniform medium at superluminal speed. The adopted formulations enrich existing HDG approaches for the solution of Maxwell's equations by including perfectly matched layers (PMLs) to effectively absorb the outgoing waves and Floquet-periodic boundary conditions to connect the boundaries of the computational domain in the direction of the moving charge. A wave propagation problem with smooth solution is used to show the optimal convergence of the HDG variables and the superconvergence of the postprocessed electric field and a second example examines the role of the PML parameters on the absorption of the electromagnetic field. A series of numerical experiments both in 3D and 2D-axisymmetric components show the capability of the proposed methods to faithfully reproduce Cherenkovian effects in different conditions and their high accuracy is confirmed by comparing the numerical results with the Frank–Tamm formula.

© 2022 Elsevier B.V. All rights reserved.

Keywords: Time domain; Frequency domain; Hybridizable discontinuous Galerkin; Cherenkov radiation; Maxwell's equations; Perfectly matched layers

1. Introduction

The Cherenkov radiation, often referred to as Vavilov–Cherenkov radiation, denotes the electromagnetic radiation generated by a charged particle moving through a medium at a speed greater than the phase velocity of light in the same medium [1]. This classical phenomenon is named after the physicist Pavel Cherenkov, who first detected the radiation under the supervision of Sergey Vavilov [2], and who shared the Nobel Prize in Physics in 1958 with Ilya Frank and Igor Tamm for its discovery and theoretical interpretation. The acoustic analogy is the sonic boom generated by an aircraft travelling at supersonic speed, which creates a characteristic shock front, named “Mach cone” if the size of the travelling object is neglected [3]. While the simulation of supersonic flows received considerable attention in the computational fluid dynamics community in the past decades and still drives the development of novel numerical strategies, the literature on the simulation of superluminal electromagnetic phenomena is rather limited.

[☆] A Special Issue in Honor of the Lifetime Achievements of J. Tinsley Oden.

^{*} Corresponding author.

E-mail address: al4188@columbia.edu (A. La Spina).

The applications of the Cherenkov radiation are disparate [4]. In particle physics, Cherenkov detectors [5] are often used to identify the charged particles by analysing the light they emit in a given medium. In nuclear engineering, the Cherenkov radiation emitted by high-energy charged particles in water can be measured to determine the radioactivity of nuclear fuel assemblies [6]. Based on the same principles, the novel Cherenkov luminescence imaging [7] allows to study radiopharmaceuticals employed for oncological uses by detecting the Cherenkov luminescence produced in human tissues. More recently, the reversed Cherenkov radiation emitted in left-handed materials has attracted the interest of researchers [8–10] and it may lead to further innovations in particle physics, astrophysics and biomolecular science and to the development of a new class of devices [11].

Our own interest in the field is aimed at understanding the Cherenkov radiation resulting from hypervelocity impact of soda-lime glass, which behaves like a highly ionized plasma in the form of charged particles moving at relativistic velocities at a temperature up to 5700 K and a pressure up to 110 GPa. Along with very sensitive sensors, an accurate description of the emitted radiation is expected to provide an estimation of the temperature at the femto-second scale, as the complex transformations involved during the impact take place [12].

The main aspect for the simulation of the Cherenkov radiation consists of the numerical solution of Maxwell's equations. Several discretization schemes have been proposed for this purpose so far. Finite difference methods for electromagnetics were introduced by the seminal work of Yee in 1966 [13] and have been widely used afterwards. Despite their computational efficiency, they are known to be inefficient on complex geometries. Finite element methods on the other hand allow to easily handle complex geometric and material configurations and they achieve high-order convergence upon mesh refinement. While conventional continuous Galerkin node-based elements can produce spurious modes [14,15], the edge-based elements introduced by Nédélec [16] provide reliable solutions to Maxwell's equations and both low- [17,18] and high- [19,20] order variants have been proposed. Discontinuous Galerkin (DG) approaches, first introduced by Reed and Hill in the context of neutron transport problems [21], have also been developed for the solution of electromagnetic problems [22–27]. They are defined over a piecewise continuous trial space and permit exchange of information among neighbouring elements through numerical fluxes defined on the element boundaries. Despite their higher-order accuracy on unstructured meshes, the flexibility in performing polynomial adaptivity (in addition to the usual mesh adaptivity) and excellent scalability properties, DG methods lead to a large number of unknowns due to the duplication of the degrees of freedom (DOFs) at the element interfaces, especially at high order of approximation. Moreover, the total number of DOFs is further increased if perfectly matched layers are added to absorb the outgoing electromagnetic waves.

More recently, hybridizable discontinuous Galerkin (HDG) methods attracted a lot of attention in the research community thanks to their capability to retain the advantages of standard DG schemes, but at a reduced computational cost. In fact, through static condensation and hybridization (guaranteed by construction [28]), HDG methods lead to a significantly smaller number of globally-coupled unknowns, in terms of the hybrid variables defined on the mesh skeleton. Moreover, an improved approximation of the solution and efficient polynomial adaptivity strategies can be devised through a computationally inexpensive postprocessing procedure [29–33]. The HDG method has been first applied to the solution of electromagnetic problems in the frequency domain by Nguyen and co-workers [34], who showed the convergence properties of the method for smooth and non-smooth two-dimensional problems equipped with essential boundary conditions. A Schwarz-type domain decomposition method has been later presented to solve the system of 3D time-harmonic Maxwell's equations [35]. The first HDG formulation for electromagnetic problems in the time domain has been developed in [36] and a variant that considers the tangential component of the electric field as hybrid variable has been later proposed in [37]. To the best of the authors' knowledge, the HDG method has never been applied to tackle superluminal electromagnetic phenomena.

On the contrary, Cherenkovian effects [38] have been traditionally treated with either finite difference-based approaches in the time domain or edge-based elements in the frequency domain. The first approach has been adopted for instance in [39–41] for the numerical simulation of the Smith–Purcell radiation and in [42,43] to study the reversed Cherenkov radiation in left-handed materials. The latter is implemented in commercial simulation software like COMSOL Multiphysics and has been used for instance in [44–46] to compute the Cherenkov radiation.

Different forms of Maxwell's equations are available in literature. The most common description of the electromagnetic field considers the electric and the magnetic vector fields and is regarded here as the “direct form”. In some circumstances it can be convenient however to solve the problem for the electric scalar potential and the magnetic vector potential, for instance when the boundary conditions are known in terms of the potentials. If the “potential form” is adopted, the physically relevant electric and magnetic fields have to be computed in

postprocessing by differentiation, thus introducing additional numerical errors. Although both forms would produce the same physical solution, we opted for the discretization of the direct form of Maxwell's equation, as it eases the treatment of the boundary conditions and returns the quantities of interest without additional calculations. This approach seems also more suitable to be integrated into a multiphysics framework [47], as required for a full-scale simulation of the emitted radiation in hypervelocity impacts.

This work presents novel HDG formulations, in both the time and the frequency domains, to accurately predict the Cherenkov radiation emitted by superluminal charged particles. Key aspects of the proposed formulations are the development of a strategy to include perfectly matched layers in the HDG framework to efficiently absorb the outgoing electromagnetic waves at a minimal computational cost and the implementation of Floquet-periodic boundary conditions to transfer the information among the boundaries in the direction of the travelling particle. Moreover, the issue of an effective treatment of the electric charge and the adoption of the axisymmetric components to reduce the computational cost of the HDG solvers are addressed in this work in the context of time- and frequency-domain electromagnetic simulations.

The remainder of this paper is organized as follows. Section 2 introduces Maxwell's equations and their discretization, together with the adopted PML formulation, in the time-domain HDG framework. The proposed HDG formulation in the frequency domain and the implementation aspects of the Floquet periodicity are then detailed in Section 3. In Section 4, the Cherenkov problem is briefly presented and the Frank–Tamm formula is derived. Section 5 presents the numerical results of the present study. The convergence properties of the time- and frequency-domain formulations are first examined on a two-dimensional wave propagation problem. A second numerical experiment investigates the role of the PML parameters on the absorption of the electromagnetic field and later the capability of the proposed solvers to accurately simulate the Cherenkov radiation in different materials is studied. The conclusions of this work are summarized in Section 6. All equations in this paper are written in the SI units.

2. HDG formulation in the time domain

2.1. Governing equations

Let $\Omega \in \mathbb{R}^{n_{sd}}$ be an open bounded domain in n_{sd} spatial dimensions. Electromagnetic phenomena are described in the time span (t_i, t_f) by Maxwell's equations

$$\begin{cases} \nabla \times \mathbf{E} = -\frac{\partial \mathbf{B}}{\partial t} & \text{in } \Omega \times (t_i, t_f), \\ \nabla \times \mathbf{H} = +\frac{\partial \mathbf{D}}{\partial t} + \mathbf{J} & \text{in } \Omega \times (t_i, t_f), \\ \nabla \cdot \mathbf{D} = \rho & \text{in } \Omega \times (t_i, t_f), \\ \nabla \cdot \mathbf{B} = 0 & \text{in } \Omega \times (t_i, t_f). \end{cases} \quad (1)$$

The first equation denotes Faraday's law in differential form, the second is referred to as Ampere–Maxwell equation, while the third and the fourth equations represent Gauss' laws for the electric and the magnetic field, respectively. The variables \mathbf{E} , \mathbf{H} , \mathbf{D} , \mathbf{B} , \mathbf{J} in (1) denote in order the electric, magnetic, electric displacement, magnetic induction and current density fields, while ρ represents the electric charge density.

For the homogeneous and isotropic materials considered in this work, the following constitutive relations are considered to describe the macroscopic properties of the medium

$$\mathbf{B} = \mu \mathbf{H}, \quad (2a)$$

$$\mathbf{D} = \varepsilon \mathbf{E}, \quad (2b)$$

$$\mathbf{J} = \sigma \mathbf{E} + \mathbf{j}, \quad (2c)$$

with μ , ε and σ being the magnetic permeability and the electric permittivity and conductivity, respectively, and \mathbf{j} denoting an external current density. In this contribution, zero conductivity is assumed, i.e. $\sigma = 0$. Moreover, Gauss' laws for the electric and the magnetic field are not included in the proposed formulations, since they are satisfied to the discretization error with the solution of Faraday's and Ampere–Maxwell equations.

In our applications, as well as in many other electromagnetic problems, the issue of modelling a domain with open boundaries arises. In this scenario, the goal is for the electromagnetic waves to pass the boundaries of the computational domain without reflection. Many approaches have been proposed in literature and the interested reader is referred to [48] for a comprehensive overview on the subject. Perfectly matched layers represent the state of the art in minimizing the wave reflection. They have been first introduced in the seminal paper by Berenger [49] in the context of finite difference time-domain simulations. The method consists of adding an extra layer surrounding the computational domain and considering an artificial permeability and permittivity to exponentially absorb all outgoing waves.

We consider the PML formulation first proposed in [50], analysed in [51] in the context of edge-based elements and later applied to the solution of wave propagation problems in metamaterials in [52]. By introducing the auxiliary fields $\tilde{\mathbf{H}}$ and $\tilde{\mathbf{E}}$, physically representing the induced magnetic and electric currents, respectively, the complete governing equations read

$$\left\{ \begin{array}{ll} \mu \frac{\partial \mathbf{H}}{\partial t} + \nabla \times \mathbf{E} + \mu \Sigma_1 \mathbf{H} + \tilde{\mathbf{H}} = \mathbf{0} & \text{in } \Omega \times (t_i, t_f), \\ \varepsilon \frac{\partial \mathbf{E}}{\partial t} - \nabla \times \mathbf{H} + \varepsilon \Sigma_1 \mathbf{E} + \tilde{\mathbf{E}} = -\mathbf{j} & \text{in } \Omega \times (t_i, t_f), \\ \frac{\partial \tilde{\mathbf{H}}}{\partial t} + \Sigma_2 \tilde{\mathbf{H}} - \mu \Sigma_3 \mathbf{H} = \mathbf{0} & \text{in } \Omega \times (t_i, t_f), \\ \frac{\partial \tilde{\mathbf{E}}}{\partial t} + \Sigma_2 \tilde{\mathbf{E}} - \varepsilon \Sigma_3 \mathbf{E} = \mathbf{0} & \text{in } \Omega \times (t_i, t_f). \end{array} \right. \quad (3)$$

The terms Σ_1 , Σ_2 and Σ_3 are diagonal matrices constructed in three dimensions as

$$\Sigma_1 = \begin{bmatrix} \sigma_y + \sigma_z - \sigma_x & 0 & 0 \\ 0 & \sigma_x + \sigma_z - \sigma_y & 0 \\ 0 & 0 & \sigma_x + \sigma_y - \sigma_z \end{bmatrix}, \quad (4a)$$

$$\Sigma_2 = \begin{bmatrix} \sigma_x & 0 & 0 \\ 0 & \sigma_y & 0 \\ 0 & 0 & \sigma_z \end{bmatrix}, \quad (4b)$$

$$\Sigma_3 = \begin{bmatrix} (\sigma_x - \sigma_y)(\sigma_x - \sigma_z) & 0 & 0 \\ 0 & (\sigma_y - \sigma_x)(\sigma_y - \sigma_z) & 0 \\ 0 & 0 & (\sigma_z - \sigma_x)(\sigma_z - \sigma_y) \end{bmatrix}, \quad (4c)$$

with σ_x , σ_y and σ_z being non-negative damping functions along the Cartesian coordinates x , y and z . The whole computational domain Ω is considered split into the PML region Ω_{PML} and the inner region Ω_{I} . The damping functions are taken positive inside the PML region and null in the inner domain and they are defined as

$$\sigma_\xi(\xi) = \begin{cases} \frac{|\xi - \xi_i|^m}{d_\xi^m} \bar{\sigma}_\xi & \text{for } \xi_i - d_\xi \leq \xi < \xi_i, \\ 0 & \text{for } \xi_i \leq \xi \leq \xi_f, \\ \frac{|\xi - \xi_f|^m}{d_\xi^m} \bar{\sigma}_\xi & \text{for } \xi_f < \xi \leq \xi_f + d_\xi, \end{cases} \quad (5)$$

along the direction ξ . In the present contribution, $\xi \in (\xi_i - d_\xi, \xi_f + d_\xi)$ can directly denote a Cartesian coordinate ($\xi \equiv x$ or y in the examples in Sections 5.1 and 5.2), or it can refer to the radial coordinate ($\xi \equiv r = \sqrt{y^2 + z^2}$ in the examples in Section 5.3). In the latter case, the damping function is split into a contribution for each Cartesian coordinate through a standard coordinate system transformation. With this notation, the parameters $\bar{\sigma}_\xi$, d_ξ and m in (5) denote a constant scaling parameter, the thickness of the PML region and a polynomial scaling factor, respectively. The numerical study in Section 5.2 shows how the thickness of the PML region can safely be taken as $d_\xi \approx \lambda/2$, with λ being the largest wavelength, whereas a polynomial scaling factor in the range $1 \leq m \leq 4$ has been observed to have a minor influence on the absorption of the electromagnetic field, unless a large ratio d/λ is considered. The scaling parameter $\bar{\sigma}_\xi$ depends instead on the discretization adopted and its value has been selected through a trial and error approach. As pointed out in [51], this formulation automatically covers all PML regions

and it is moreover able to recover the standard Maxwell equations by setting $\Sigma_1 = \Sigma_2 = \Sigma_3 = \mathbf{0}$ and interpreting $\tilde{\mathbf{H}}$ and $\tilde{\mathbf{E}}$ as external current sources.

2.2. Initial and boundary conditions

The electromagnetic problem defined by Eqs. (3) needs to be completed with suitable initial and boundary conditions. The initial fields

$$\mathbf{H}^0 = \mathbf{H}(x, y, z, t_i), \quad (6a)$$

$$\mathbf{E}^0 = \mathbf{E}(x, y, z, t_i), \quad (6b)$$

$$\tilde{\mathbf{H}}^0 = \tilde{\mathbf{H}}(x, y, z, t_i), \quad (6c)$$

$$\tilde{\mathbf{E}}^0 = \tilde{\mathbf{E}}(x, y, z, t_i), \quad (6d)$$

satisfying the problem (3) at $t = t_i$ are provided. In all the numerical examples presented here, the electromagnetic fields are initialized with homogeneous functions in the whole domain.

Different types of boundary conditions are considered in this contribution. Dirichlet boundary conditions prescribe the tangential component of the electric field to a given value \mathbf{E}_t^D as

$$\mathbf{n} \times \mathbf{E} = \mathbf{E}_t^D, \quad (7)$$

where \mathbf{n} denotes the outward-pointing unit normal vector to the boundary. Perfect electric conductor (PEC) boundary conditions, simulating boundaries that behave as perfect electric conductors (such as metals), can be easily embedded, since they constitute a special case of the condition (7) for which $\mathbf{E}_t^D = \mathbf{0}$. The so-called perfect magnetic conductor (PMC) conditions represent the magnetic equivalent of the PEC conditions and they prescribe a zero tangential component of the magnetic field as

$$\mathbf{n} \times \mathbf{H} = \mathbf{0}. \quad (8)$$

Although no substantial differences have been observed by terminating the PML region with either PEC or absorbing boundary conditions (ABC), a first-order approximation of the Silver–Müller condition [53] is considered. Appreciable differences between the two alternatives can instead be observed for a very small PML thickness [54]. The Silver–Müller condition can be expressed in terms of the total magnetic and electric fields as

$$-\mathbf{n} \times \mathbf{H} - \sqrt{\frac{\varepsilon}{\mu}} \mathbf{n} \times \mathbf{E} \times \mathbf{n} = \mathbf{g}, \quad (9)$$

with \mathbf{g} denoting the incident field.

Periodic boundary conditions are considered in the time-domain formulation to connect the boundaries of the computational domain in the direction of the moving charge. Such conditions have been adopted in the HDG framework for the solution of other physical problems [55,56]. For our specific applications, the periodic boundary conditions applied on the x -direction require that

$$\mathbf{H}(x + L, y, z, t) = \mathbf{H}(x, y, z, t), \quad (10a)$$

$$\mathbf{E}(x + L, y, z, t) = \mathbf{E}(x, y, z, t), \quad (10b)$$

with L being the length of the computational domain in the direction of the travelling charge. To apply the periodic boundary conditions to the left and right side of the domain boundary, we define a primary and a replica portion and we assume a conforming discretization on such portions. In the pre-processing step, the global faces and degrees of freedom are rearranged such that the faces belonging to the periodic portion of the boundary effectively behave as internal faces, whose orientation is dictated by the orientation of the faces on the primary side. Special considerations hold however for the implementation of the Floquet-periodic boundary conditions in the frequency domain, as explained in Section 3.

2.3. Strong form

To derive the strong form of the proposed time-domain HDG formulation, the whole computational domain $\Omega = \Omega_I \cup \Omega_{\text{PML}}$ is partitioned into n^{el} disjoint elements as

$$\Omega = \bigcup_{e=1}^{n^{\text{el}}} \Omega^e, \quad \text{with} \quad \Omega^e \cap \Omega^f = \emptyset \quad \text{for} \quad e \neq f. \quad (11)$$

The boundary of the computational domain is considered split into three portions $\partial\Omega = \Gamma^D \cup \Gamma^A \cup \Gamma^P$ corresponding to the regions where Dirichlet, absorbing and periodic boundary conditions are applied, respectively. The internal interface Γ collects the internal faces, whereas the mesh skeleton Σ includes all the faces in which the global trace variable is sought, and they are defined as

$$\Gamma = \left[\bigcup_{e=1}^{n^{\text{el}}} \partial\Omega^e \right] \setminus \partial\Omega, \quad \Sigma = \left[\bigcup_{e=1}^{n^{\text{el}}} \partial\Omega^e \right] \setminus \Gamma^D. \quad (12)$$

The problem (3) can therefore be written over the broken computational domain as

$$\left\{ \begin{array}{ll} \mu \frac{\partial \mathbf{H}}{\partial t} + \nabla_{\mathbf{w}} \mathbf{E} + \mu \Sigma_1 \mathbf{H} + \tilde{\mathbf{H}} = \mathbf{0} & \text{in } \Omega^e \times (t_i, t_f), \\ \varepsilon \frac{\partial \mathbf{E}}{\partial t} + \nabla_{\mathbf{w}}^T \mathbf{H} + \varepsilon \Sigma_1 \mathbf{E} + \tilde{\mathbf{E}} = -\mathbf{j} & \text{in } \Omega^e \times (t_i, t_f), \\ \frac{\partial \tilde{\mathbf{H}}}{\partial t} + \Sigma_2 \tilde{\mathbf{H}} - \mu \Sigma_3 \mathbf{H} = \mathbf{0} & \text{in } \Omega^e \times (t_i, t_f), \\ \frac{\partial \tilde{\mathbf{E}}}{\partial t} + \Sigma_2 \tilde{\mathbf{E}} - \varepsilon \Sigma_3 \mathbf{E} = \mathbf{0} & \text{in } \Omega^e \times (t_i, t_f), \\ \mathbf{H} = \mathbf{H}^0, \quad \mathbf{E} = \mathbf{E}^0, \quad \tilde{\mathbf{H}} = \tilde{\mathbf{H}}^0, \quad \tilde{\mathbf{E}} = \tilde{\mathbf{E}}^0 & \text{in } \Omega^e \times (t_i), \\ \mathbf{E}_t = \widehat{\mathbf{E}}_t & \text{on } \partial\Omega^e \setminus \Gamma^D \times (t_i, t_f), \\ \mathbf{E}_t = \mathbf{E}_t^D & \text{on } \partial\Omega^e \cap \Gamma^D \times (t_i, t_f), \end{array} \right. \quad (13)$$

for $e = 1, \dots, n^{\text{el}}$. The local problems (13) allow to compute the local quantities $(\mathbf{H}, \mathbf{E}, \tilde{\mathbf{H}}, \tilde{\mathbf{E}})$ in terms of the global variable $\widehat{\mathbf{E}}_t$, consisting of the tangential component of the electric field on the mesh skeleton Σ . The local problems moreover include the initial conditions on the primal and the auxiliary fields at $t = t_i$ and they embed the essential boundary conditions on the element boundaries $\partial\Omega^e$ (last two conditions). The operator $\nabla_{\mathbf{w}}$ has size $q_{\text{sd}} \times n_{\text{sd}}$ (with $q_{\text{sd}} = 1$ in 2D and $q_{\text{sd}} = 3$ in 3D) and computes the curl of either the magnetic or the electric field. It is defined as

$$\nabla_{\mathbf{w}} = \left\{ \begin{array}{ll} \begin{bmatrix} -\partial/\partial y & \partial/\partial x \\ 0 & -\partial/\partial z & \partial/\partial y \\ \partial/\partial z & 0 & -\partial/\partial x \end{bmatrix} & \text{in 2D (TE mode),} \\ \begin{bmatrix} -\partial/\partial y & \partial/\partial x & 0 \end{bmatrix} & \text{in 3D,} \end{array} \right. \quad (14)$$

and it allows to generalize the formulation to include three-dimensional problems in the local unknowns $(H_x, H_y, H_z, E_x, E_y, E_z, \tilde{H}_x, \tilde{H}_y, \tilde{H}_z, \tilde{E}_x, \tilde{E}_y, \tilde{E}_z)$ and two-dimensional problems in the transverse electric (TE) mode with the local unknowns $(H_z, E_x, E_y, \tilde{H}_z, \tilde{E}_x, \tilde{E}_y)$.

The global problem consists of the transmission conditions, enforcing the continuity of the tangential component of the electric field and the equilibrium of the numerical fluxes across the internal interface Γ . It moreover embeds the absorbing boundary conditions on Γ^A . The global problem thus reads

$$\left\{ \begin{array}{ll} \llbracket \mathbf{T} \mathbf{E} \rrbracket = \mathbf{0} & \text{on } \Gamma \times (t_i, t_f), \\ \llbracket \widehat{\mathbf{T}^T \mathbf{H}} \rrbracket = \mathbf{0} & \text{on } \Gamma \times (t_i, t_f), \\ \mathbf{T}^T \mathbf{H} - \sqrt{\frac{\varepsilon}{\mu}} \mathbf{R} \mathbf{E}_t = \mathbf{g} & \text{on } \Gamma^A \times (t_i, t_f). \end{array} \right. \quad (15)$$

The tangent operator \mathbf{T} is defined as $\nabla_{\mathbf{w}}$, with the partial derivatives with respect to the coordinates x , y and z replaced by the components of the normal vector n_x , n_y and n_z , respectively, whereas \mathbf{R} is a $\mathbf{n}_{\text{sd}} \times (\mathbf{n}_{\text{sd}} - 1)$ operator constructed via the Gram–Schmidt orthonormalization process that allows to transform vectors from the face reference frame to the domain reference frame (and vice-versa) [57,58]. In fact, the electric field \mathbf{E} has \mathbf{n}_{sd} components, whereas the tangential component \mathbf{E}_t is henceforth expressed in terms of $\mathbf{n}_{\text{sd}} - 1$ components in the face reference frame. Moreover, the jump operator defined in [59] sums values from two adjacent elements Ω^e and Ω^f as

$$[\![\odot]\!] = \odot^e + \odot^f. \quad (16)$$

It is worth pointing out that the first condition in (15) is automatically satisfied, owing to the essential boundary conditions in (13) and the unique definition of the hybrid variable on each face of the mesh skeleton. Moreover, the flux equilibrium is accounted for by the adoption of the following numerical fluxes

$$\widehat{\mathbf{T}^T \mathbf{H}} = \begin{cases} \mathbf{T}^T \mathbf{H} + \tau_t (\mathbf{T}^T \mathbf{T} \mathbf{E} - \mathbf{R} \widehat{\mathbf{E}}_t) & \text{on } \partial \Omega^e \setminus \Gamma^D \times (t_i, t_f), \\ \mathbf{T}^T \mathbf{H} + \tau_t (\mathbf{T}^T \mathbf{T} \mathbf{E} - \mathbf{R} \mathbf{E}_t^D) & \text{on } \partial \Omega^e \cap \Gamma^D \times (t_i, t_f), \end{cases} \quad (17)$$

with τ_t being a stabilization parameter, whose crucial role in the accuracy and convergence of the HDG method has been investigated by many authors [28,60–64].

2.4. Weak form

The following functional spaces are defined for the approximation of the test and the trial functions

$$\mathcal{V}^h(\Omega) = \{ \mathbf{v} \in \mathcal{L}^2(\Omega) : \mathbf{v}|_{\Omega^e} \in \mathcal{P}^k(\Omega^e) \forall \Omega^e \subset \Omega \}, \quad (18a)$$

$$\widehat{\mathcal{V}}^h(\Sigma) = \{ \widehat{\mathbf{v}} \in \mathcal{L}^2(\Sigma) : \widehat{\mathbf{v}}|_{\Sigma^f} \in \mathcal{P}^k(\Sigma^f) \forall \Sigma^f \subset \Sigma \}, \quad (18b)$$

with \mathcal{P}^k denoting the space of polynomial functions of complete degree at most k . Moreover, the \mathcal{L}^2 inner products for vector-valued functions on the generic element Ω^e or face Σ^f are defined as

$$(\mathbf{u}, \mathbf{v})_{\Omega^e} = \int_{\Omega^e} \mathbf{u} \cdot \mathbf{v} \, d\Omega, \quad \langle \mathbf{u}, \mathbf{v} \rangle_{\Sigma^f} = \int_{\Sigma^f} \mathbf{u} \cdot \mathbf{v} \, d\Sigma. \quad (19)$$

To obtain the weak form of the HDG local problems, the governing equations in (13) are multiplied by the test functions and integrated over the elemental domains. By performing a single integration by parts on the magnetic field equation and a double integration by parts on the electric field equation and by inserting the definition of the numerical fluxes (17), the local problems can be stated as: given $(\mathbf{H}^0, \mathbf{E}^0, \widetilde{\mathbf{H}}^0, \widetilde{\mathbf{E}}^0)$ in $\Omega^e \times (t_i, t_f)$, \mathbf{E}_t^D on Γ^D and $\widehat{\mathbf{E}}_t$ on Σ , find $(\mathbf{H}, \mathbf{E}, \widetilde{\mathbf{H}}, \widetilde{\mathbf{E}}) \in [\mathcal{V}^h(\Omega^e)]^{\text{qsd}} \times [\mathcal{V}^h(\Omega^e)]^{\text{nsd}} \times [\mathcal{V}^h(\Omega^e)]^{\text{qsd}} \times [\mathcal{V}^h(\Omega^e)]^{\text{nsd}}$ for $e = 1, \dots, \mathbf{n}^{\text{el}}$ such that

$$-\left(\mathbf{V}, \mu \frac{\partial \mathbf{H}}{\partial t} \right)_{\Omega^e} + (\nabla_{\mathbf{w}}^T \mathbf{V}, \mathbf{E})_{\Omega^e} - (\mathbf{V}, \mu \Sigma_1 \mathbf{H})_{\Omega^e} - (\mathbf{V}, \widetilde{\mathbf{H}})_{\Omega^e} = \langle \mathbf{T}^T \mathbf{V}, \mathbf{R} \widehat{\mathbf{E}}_t \rangle_{\partial \Omega^e \setminus \Gamma^D} + \langle \mathbf{T}^T \mathbf{V}, \mathbf{R} \mathbf{E}_t^D \rangle_{\partial \Omega^e \cap \Gamma^D}, \quad (20a)$$

$$\left(\mathbf{v}, \varepsilon \frac{\partial \mathbf{E}}{\partial t} \right)_{\Omega^e} + (\mathbf{v}, \nabla_{\mathbf{w}}^T \mathbf{H})_{\Omega^e} + (\mathbf{v}, \varepsilon \Sigma_1 \mathbf{E})_{\Omega^e} + (\mathbf{v}, \widetilde{\mathbf{E}})_{\Omega^e} + (\mathbf{v}, \mathbf{j})_{\Omega^e} = -\langle \mathbf{T} \mathbf{v}, \tau_t \mathbf{T} \mathbf{E} \rangle_{\partial \Omega^e} + \langle \mathbf{v}, \tau_t \mathbf{R} \widehat{\mathbf{E}}_t \rangle_{\partial \Omega^e \setminus \Gamma^D} + \langle \mathbf{v}, \tau_t \mathbf{R} \mathbf{E}_t^D \rangle_{\partial \Omega^e \cap \Gamma^D}, \quad (20b)$$

$$\left(\mathbf{W}, \frac{\partial \widetilde{\mathbf{H}}}{\partial t} \right)_{\Omega^e} + (\mathbf{W}, \Sigma_2 \widetilde{\mathbf{H}})_{\Omega^e} - (\mathbf{W}, \mu \Sigma_3 \mathbf{H})_{\Omega^e} = 0, \quad (20c)$$

$$-\left(\mathbf{w}, \frac{\partial \widetilde{\mathbf{E}}}{\partial t} \right)_{\Omega^e} - (\mathbf{w}, \Sigma_2 \widetilde{\mathbf{E}})_{\Omega^e} + (\mathbf{w}, \varepsilon \Sigma_3 \mathbf{E})_{\Omega^e} = 0, \quad (20d)$$

for all $(\mathbf{V}, \mathbf{v}, \mathbf{W}, \mathbf{w}) \in [\mathcal{V}^h(\Omega^e)]^{\text{qsd}} \times [\mathcal{V}^h(\Omega^e)]^{\text{nsd}} \times [\mathcal{V}^h(\Omega^e)]^{\text{qsd}} \times [\mathcal{V}^h(\Omega^e)]^{\text{nsd}}$. It is worth noting that the essential boundary conditions, imposing either the Dirichlet data \mathbf{E}_t^D on $\partial \Omega^e \cap \Gamma^D$ or the trace variable $\widehat{\mathbf{E}}_t$ on $\partial \Omega^e \setminus \Gamma^D$, are enforced in a weak sense in (20).

The HDG global problem is derived by replacing the definitions (17) in the transmission conditions in (15) and by inserting the absorbing boundary conditions (9). Its weak form reads: given \mathbf{g} on Γ^A , find $\widehat{\mathbf{E}}_t \in [\widehat{\mathcal{V}}^h(\Sigma)]^{n_{sd}-1}$ such that

$$\sum_{e=1}^{n_{el}} \left\{ -\langle \mathbf{R}\hat{\mathbf{v}}_t, \mathbf{T}^T \mathbf{H} \rangle_{\partial\Omega^e \setminus \Gamma^D} - \langle \mathbf{R}\hat{\mathbf{v}}_t, \tau_t \mathbf{E} \rangle_{\partial\Omega^e \setminus \Gamma^D} + \langle \mathbf{R}\hat{\mathbf{v}}_t, \tau_t \mathbf{R}\widehat{\mathbf{E}}_t \rangle_{\partial\Omega^e \setminus \Gamma^D} \right. \\ \left. + \left\langle \mathbf{R}\hat{\mathbf{v}}_t, \sqrt{\frac{\varepsilon}{\mu}} \mathbf{R}\widehat{\mathbf{E}}_t \right\rangle_{\partial\Omega^e \cap \Gamma^A} \right\} = - \sum_{e=1}^{n_{el}} \langle \mathbf{R}\hat{\mathbf{v}}_t, \mathbf{g} \rangle_{\partial\Omega^e \cap \Gamma^A}, \quad (21)$$

for all $\hat{\mathbf{v}}_t \in [\widehat{\mathcal{V}}^h(\Sigma)]^{n_{sd}-1}$. Although not used in this work, the perfectly magnetic conditions (8) are naturally imposed in the global problem of our formulation, owing to the transmission conditions in (15) and to the definition of the fluxes in (17).

Compared to the HDG discretization of the pure Maxwell equations [36,37], the adopted PML formulation adds two ordinary differential equations in the local problems (20). An interesting feature in including perfectly matched layers in the HDG framework is that the additional equations can be solved locally and do not affect the size of the resulting global system. In fact, whereas the total number of components of the unknown variables in the local problems increases from $q_{sd} + n_{sd}$ to $2(q_{sd} + n_{sd})$, the number of components in the global problem remains unaltered and equal to $n_{sd} - 1$. Note that the increase of the dimension of the local problems has a negligible effect on the total computational time, since the problems (20) are solved in parallel in an element-by-element fashion and most of the computational time is spent on the solution of the global problem (21). As a consequence, the main source of increase of the computational effort of the proposed approach compared to the formulations in [36,37] can be attributed to the slight increase of the number of elements needed to discretize the PML region.

For the temporal integration, the second-order backward differentiation formula (BDF2), initialized with the backward Euler method at the first time step, is adopted. The implicit nature of this linear multistep method allows to determine the time step size solely via accuracy considerations and it is thus not subjected to the restrictions classically imposed by explicit methods.

2.5. Axisymmetric formulation

In Section 5.3, an axisymmetric formulation is considered to simulate the Cherenkov radiation emitted by a charge travelling in the x -direction. Such formulation exploits the rotational symmetry around the x -axis to reduce the three-dimensional problem into a two-dimensional one, drastically reducing the number of unknowns and saving both memory and time. The cylindrical coordinates (x, r, θ) are related to the Cartesian coordinates (x, y, z) by

$$\begin{cases} x = x, \\ r = \sqrt{y^2 + z^2}, \\ \theta = \text{atan2}(z, y), \end{cases} \quad (22)$$

with atan2 denoting the four-quadrant inverse tangent, returning values in the interval $(-\pi, +\pi)$. The curl operator in the cylindrical coordinates so defined reads

$$\nabla \times \mathbf{u} = \begin{bmatrix} \frac{1}{r} \frac{\partial(r u_\theta)}{\partial r} - \frac{1}{r} \frac{\partial u_r}{\partial \theta} \\ \frac{1}{r} \frac{\partial u_x}{\partial \theta} - \frac{\partial u_\theta}{\partial x} \\ \frac{\partial u_r}{\partial x} - \frac{\partial u_x}{\partial r} \end{bmatrix}, \quad (23)$$

for the generic variable \mathbf{u} . In axisymmetric conditions, the solution is invariant in θ , i.e. $\partial/\partial\theta = 0$, and the magnetic and electric fields reduce to $\mathbf{H} = [0, 0, H_\theta(x, r)]^T$ and $\mathbf{E} = [E_x(x, r), E_r(x, r), 0]^T$. In such scenario, the curl

operator applied to the electromagnetic fields reads

$$\nabla \times \mathbf{H} = \begin{bmatrix} \frac{\partial H_\theta}{\partial r} + \frac{1}{r} H_\theta \\ -\frac{\partial H_\theta}{\partial x} \\ 0 \end{bmatrix}, \quad \nabla \times \mathbf{E} = \begin{bmatrix} 0 \\ 0 \\ \frac{\partial E_r}{\partial x} - \frac{\partial E_x}{\partial r} \end{bmatrix}. \quad (24)$$

From the definitions (22) and (24) it is straightforward to demonstrate that the axisymmetric solution of Eqs. (3) can be obtained by solving the standard 2D problem (TE mode) in the Cartesian coordinates with the inclusion of the extra term $\frac{1}{y} H_z$ in the right hand side of the E_x equation. The local problems (13) can therefore be written in axisymmetric conditions as

$$\left\{ \begin{array}{l} \mu \frac{\partial H_z}{\partial t} + \frac{\partial E_y}{\partial x} - \frac{\partial E_x}{\partial y} + \mu(\sigma_x + \sigma_y) H_z + \tilde{H}_z = 0, \\ \varepsilon \frac{\partial E_x}{\partial t} - \frac{\partial H_z}{\partial y} + \varepsilon(\sigma_y - \sigma_x) E_x + \tilde{E}_x = -j_x + \frac{1}{y} H_z, \\ \varepsilon \frac{\partial E_y}{\partial t} + \frac{\partial H_z}{\partial x} + \varepsilon(\sigma_x - \sigma_y) E_y + \tilde{E}_y = -j_y, \\ \frac{\partial \tilde{H}_z}{\partial t} - \mu \sigma_x \sigma_y H_z = 0, \\ \frac{\partial \tilde{E}_x}{\partial t} + \sigma_x \tilde{E}_x - \varepsilon(\sigma_x - \sigma_y) \sigma_x E_x = 0, \\ \frac{\partial \tilde{E}_y}{\partial t} + \sigma_y \tilde{E}_y - \varepsilon(\sigma_y - \sigma_x) \sigma_y E_y = 0, \end{array} \right. \quad (25)$$

with the addition of the initial and the boundary conditions. The global problem, not containing any differential operator, remains unchanged instead.

2.6. Postprocessing

A key advantage of the HDG method over alternative discretization approaches is the possibility to exploit the optimal convergence of the local variables to construct an improved approximation of the solution, converging with an additional order of accuracy. For the proposed formulation, a postprocessing strategy produces an approximation of the electric field \mathbf{E}^* superconverging in the $\mathcal{H}^{\text{curl}}$ norm with order $k+1$, whereas the original solution \mathbf{E} converges in the same norm with order k . The following richer spaces are introduced

$$\mathcal{V}_\star^h(\Omega) = \{ \mathbf{v}^\star \in \mathcal{L}^2(\Omega) : \mathbf{v}^\star|_{\Omega^e} \in \mathcal{P}^{k+1}(\Omega^e) \forall \Omega^e \subset \Omega \}, \quad (26a)$$

$$\mathcal{V}_{\star\star}^h(\Omega) = \{ \mathbf{v}^{\star\star} \in \mathcal{L}^2(\Omega) : \mathbf{v}^{\star\star}|_{\Omega^e} \in \mathcal{P}^{k+2}(\Omega^e) \forall \Omega^e \subset \Omega \}. \quad (26b)$$

The postprocessed solution is sought in the first space in (26), whereas the second functional space is introduced to remove the underdetermination of the problem. The weak form of the proposed postprocessing strategy reads: given $(\mathbf{H}, \mathbf{E}, \tilde{\mathbf{H}})$ in Ω^e , find $\mathbf{E}^\star \in [\mathcal{V}_\star^h(\Omega^e)]^{\text{n}_{\text{sd}}}$ for $e = 1, \dots, \text{n}^{\text{el}}$ such that

$$-(\nabla_{\mathbf{w}} \mathbf{v}^\star, \nabla_{\mathbf{w}} \mathbf{E}^\star)_{\Omega^e} = \left(\nabla_{\mathbf{w}} \mathbf{v}^\star, \mu \frac{\partial \mathbf{H}}{\partial t} \right)_{\Omega^e} + (\nabla_{\mathbf{w}} \mathbf{v}^\star, \mu \Sigma_1 \mathbf{H})_{\Omega^e} + (\nabla_{\mathbf{w}} \mathbf{v}^\star, \tilde{\mathbf{H}})_{\Omega^e}, \quad (27a)$$

$$(\nabla \mathbf{v}^{\star\star}, \mathbf{E}^\star)_{\Omega^e} = (\nabla \mathbf{v}^{\star\star}, \mathbf{E})_{\Omega^e}, \quad (27b)$$

for all $(\mathbf{v}^\star, \mathbf{v}^{\star\star}) \in [\mathcal{V}_\star^h(\Omega^e)]^{\text{n}_{\text{sd}}} \times \mathcal{V}_{\star\star}^h(\Omega^e)$. The first equation directly follows from the equation of the magnetic field in (13), whereas the last condition ensures the solvability of the problem. Eqs. (27) can be easily solved in parallel at the time steps in which an improved solution is desired and, although not addressed in this work, the difference between the original and the postprocessed solution can be exploited to drive efficient polynomial adaptivity strategies.

3. HDG formulation in the frequency domain

While the time-domain formulation in Section 2 can be adopted to compute the Cherenkov radiation emitted by a charged particle over a range of frequencies, dictated by the time span and the time step size considered, the solution of a frequency-domain problem returns information relative to a unique frequency f . The frequency-domain counterpart of the time-domain problem (3) can be obtained by assuming a time-periodic solution and thus replacing the temporal derivatives with $i\omega$, with i denoting the imaginary unit and $\omega = 2\pi f$ the angular frequency. With this formalism, the equations on the auxiliary fields $\tilde{\mathbf{E}}$ and $\tilde{\mathbf{H}}$ can be eliminated and their effect is taken into account by means of additional terms in the equations of the magnetic and electric fields as

$$\begin{cases} i\mu\omega\mathbf{H} + \nabla \times \mathbf{E} + \mu\Sigma_*(\omega)\mathbf{H} = \mathbf{0} & \text{in } \Omega \times \omega, \\ i\varepsilon\omega\mathbf{E} - \nabla \times \mathbf{H} + \varepsilon\Sigma_*(\omega)\mathbf{E} = -\mathbf{j} & \text{in } \Omega \times \omega, \end{cases} \quad (28)$$

where $\Sigma_*(\omega) = \Sigma_1 + (i\omega\mathbf{I} + \Sigma_2)^{-1}\Sigma_3$.

The same rationale of Section 2.3 is adopted to derive the strong form of the local and global problems of the frequency-domain formulation, but the procedure is not repeated to avoid redundancy. The weak form of the local problems instead reads: given \mathbf{E}_t^D on Γ^D and $\hat{\mathbf{E}}_t$ on Σ , find $(\mathbf{H}, \mathbf{E}) \in [\mathcal{V}^h(\Omega^e)]^{\text{qsd}} \times [\mathcal{V}^h(\Omega^e)]^{\text{n sd}}$ for $e = 1, \dots, n^{\text{el}}$ such that

$$-(\mathbf{V}, i\mu\omega\mathbf{H})_{\Omega^e} + (\nabla_{\mathbf{w}}^T \mathbf{V}, \mathbf{E})_{\Omega^e} - (\mathbf{V}, \mu\Sigma_*(\omega)\mathbf{H})_{\Omega^e} = \langle \mathbf{T}^T \mathbf{V}, \mathbf{R}\hat{\mathbf{E}}_t \rangle_{\partial\Omega^e \setminus \Gamma^D} + \langle \mathbf{T}^T \mathbf{V}, \mathbf{R}\mathbf{E}_t^D \rangle_{\partial\Omega^e \cap \Gamma^D}, \quad (29a)$$

$$(\mathbf{v}, i\varepsilon\omega\mathbf{E})_{\Omega^e} + (\mathbf{v}, \nabla_{\mathbf{w}}^T \mathbf{H})_{\Omega^e} + (\mathbf{v}, \varepsilon\Sigma_*(\omega)\mathbf{E})_{\Omega^e} + (\mathbf{v}, \mathbf{j})_{\Omega^e} = -\langle \mathbf{T}\mathbf{v}, \tau_{\omega}\mathbf{E} \rangle_{\partial\Omega^e} + \langle \mathbf{v}, \tau_{\omega}\mathbf{R}\hat{\mathbf{E}}_t \rangle_{\partial\Omega^e \setminus \Gamma^D} + \langle \mathbf{v}, \tau_{\omega}\mathbf{R}\mathbf{E}_t^D \rangle_{\partial\Omega^e \cap \Gamma^D}, \quad (29b)$$

for all $(\mathbf{V}, \mathbf{v}) \in [\mathcal{V}^h(\Omega^e)]^{\text{qsd}} \times [\mathcal{V}^h(\Omega^e)]^{\text{n sd}}$. It is worth noting that the problems (29) produce symmetric matrices with complex entries that can be efficiently solved by ad-hoc solvers. However, the adoption of the Floquet-periodic boundary conditions introduce some modifications in (29). Such boundary conditions consider a phase shift of the solution, determined by a wave vector and the distance between the source and the destination, and they state that

$$\mathbf{H}(x + L, y, z, \omega) = \mathbf{H}(x, y, z, \omega)e^{-ik_F L}, \quad (30a)$$

$$\mathbf{E}(x + L, y, z, \omega) = \mathbf{E}(x, y, z, \omega)e^{-ik_F L}, \quad (30b)$$

if the charged particle is considered travelling in the x -direction. The Floquet vector is computed as $k_F = \omega/v$, with v being the particle velocity. An arbitrary value can be considered for the distance L between the source and the destination when analysing the Cherenkov radiation in a uniform medium, and it is here selected as the length of the computational domain in the direction of the travelling charge. However, its value must equal the periodicity of the refractive index if a non-uniform periodic medium (such as an infinite grating) is considered [65]. To include the Floquet-periodic boundary conditions with minimal changes, the following function is introduced

$$\chi_F = \begin{cases} e^{-ik_F L} & \text{on } \Gamma_R^P, \\ 1 & \text{elsewhere,} \end{cases} \quad (31)$$

with Γ_R^P denoting the replica side of the periodic boundary portion Γ^P . In fact, according to the strategy presented in Section 2.2 to handle periodic-type boundary conditions in the HDG framework, and by considering the equalities (30), the electromagnetic fields on the primary (with subscript \odot_P) and the replica (with subscript \odot_R) sides are related by

$$\mathbf{H}_R = \mathbf{H}_P \chi_F, \quad (32a)$$

$$\mathbf{E}_R = \mathbf{E}_P \chi_F, \quad (32b)$$

by assuming the primary side coinciding with the source and the replica side with the destination. With this notation, the local and the global problems can be generalized to account for Floquet-periodic boundary conditions as follows. The weak form of the local problems reads: given \mathbf{E}_t^D on Γ^D and $\hat{\mathbf{E}}_t$ on Σ , find $(\mathbf{H}, \mathbf{E}) \in [\mathcal{V}^h(\Omega^e)]^{\text{qsd}} \times [\mathcal{V}^h(\Omega^e)]^{\text{n sd}}$

for $e = 1, \dots, n^{el}$ such that

$$-(V, i\mu\omega H)_{\Omega^e} + (\nabla_w^T V, E)_{\Omega^e} - (V, \mu\Sigma_*(\omega)H)_{\Omega^e} = \langle T^T V, R\hat{E}_t \chi_F \rangle_{\partial\Omega^e \setminus \Gamma^D} + \langle T^T V, RE_t^D \rangle_{\partial\Omega^e \cap \Gamma^D}, \quad (33a)$$

$$(v, i\varepsilon\omega E)_{\Omega^e} + (v, \nabla_w^T H)_{\Omega^e} + (v, \varepsilon\Sigma_*(\omega)E)_{\Omega^e} + (v, j)_{\Omega^e} = -\langle Tv, \tau_\omega TE \rangle_{\partial\Omega^e} + \langle v, \tau_\omega R\hat{E}_t \chi_F \rangle_{\partial\Omega^e \setminus \Gamma^D} + \langle v, \tau_\omega RE_t^D \rangle_{\partial\Omega^e \cap \Gamma^D}, \quad (33b)$$

for all $(V, v) \in [\mathcal{V}^h(\Omega^e)]^{qsd} \times [\mathcal{V}^h(\Omega^e)]^{nsd}$. The weak form of the global problem instead reads: given g on Γ^A , find $\hat{E}_t \in [\hat{\mathcal{V}}^h(\Sigma)]^{nsd-1}$ such that

$$\sum_{e=1}^{n^{el}} \left\{ -\langle R\hat{v}_t, T^T H \chi_F^{-1} \rangle_{\partial\Omega^e \setminus \Gamma^D} - \langle R\hat{v}_t, \tau_\omega E \chi_F^{-1} \rangle_{\partial\Omega^e \setminus \Gamma^D} + \langle R\hat{v}_t, \tau_\omega R\hat{E}_t \rangle_{\partial\Omega^e \setminus \Gamma^D} + \left\langle R\hat{v}_t, \sqrt{\frac{\varepsilon}{\mu}} R\hat{E}_t \right\rangle_{\partial\Omega^e \cap \Gamma^A} \right\} = - \sum_{e=1}^{n^{el}} \langle R\hat{v}_t, g \rangle_{\partial\Omega^e \cap \Gamma^A}, \quad (34)$$

for all $\hat{v}_t \in [\hat{\mathcal{V}}^h(\Sigma)]^{nsd-1}$. It is worth noting that, since the trace DOFs are suppressed on the replica side (destination) and they are considered belonging to the primary side (source), the global variable \hat{E}_t is scaled by the quantity χ_F in the local problems (33), whereas the local variables H and E are scaled by χ_F^{-1} to properly account for the transmission conditions in the global problem (34). The postprocessing strategy is analogous to the time-domain counterpart (27) and reads: given (H, E) in Ω^e , find $E^* \in [\mathcal{V}_*^h(\Omega^e)]^{nsd}$ for $e = 1, \dots, n^{el}$ such that

$$-(\nabla_w v^*, \nabla_w E^*)_{\Omega^e} = (\nabla_w v^*, i\mu\omega H)_{\Omega^e} + (\nabla_w v^*, \mu\Sigma_*(\omega)H)_{\Omega^e}, \quad (35a)$$

$$(\nabla_v v^{**}, E^*)_{\Omega^e} = (\nabla_v v^{**}, E)_{\Omega^e}, \quad (35b)$$

for all $(v^*, v^{**}) \in [\mathcal{V}_*^h(\Omega^e)]^{nsd} \times \mathcal{V}_{**}^h(\Omega^e)$.

4. Cherenkov radiation and Frank–Tamm formula

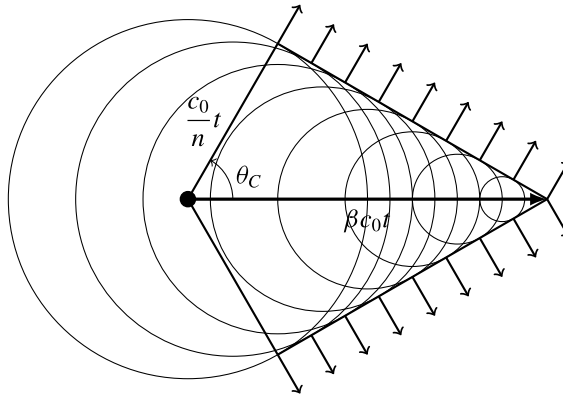


Fig. 1. Schematic representation of the Cherenkov radiation.

The focus of this contribution is the accurate simulation of the Cherenkov radiation by means of hybridizable discontinuous Galerkin solvers, presented in Sections 2 and 3 in the context of time- and frequency-domain frameworks. Although the Cherenkov radiation is a classical electromagnetic phenomenon, described for instance in [1], its concept is briefly recalled here to better contextualize the results in Section 5.3. The scenario simulated considers a particle with charge q moving in the x -direction at constant velocity $v = \beta c_0$. The speed of light is computed as $c_0 = 1/\sqrt{\varepsilon_0\mu_0}$, with ε_0 and μ_0 denoting the electric permittivity and the magnetic permeability in vacuum, respectively. The medium is thus characterized by a permeability $\mu = \mu_0$ and a refractive index $n = \sqrt{\varepsilon/\varepsilon_0}$,

considered frequency-independent. A point-like particle can be modelled by the current density

$$j_x(x, y, z, t) = qv\delta(x - vt)\delta(y)\delta(z), \quad (36)$$

with δ denoting the Dirac delta function. No radiation is emitted if the particle velocity is less than the phase velocity of light in the medium, i.e. $v < c_0/n$. However, for $v > c_0/n$, the spherical wavelets shown in Fig. 1 interfere constructively emitting the so-called Cherenkov radiation, travelling at speed c_0/n at an angle $\theta_C = \arccos(\frac{1}{\beta n})$ with respect to the particle trajectory.

The solution of the Cherenkov problem in terms of the magnetic and electric potentials A and Φ in the cylindrical coordinates (x, r, θ) in the frequency domain reads [66]

$$A = \begin{bmatrix} \frac{q\mu}{4\pi^2} K_0 \left(i \frac{\omega}{v} r \sqrt{\beta^2 n^2 - 1} \right) e^{-i \frac{\omega}{v} x} \\ 0 \\ 0 \end{bmatrix}, \quad (37a)$$

$$\Phi = \frac{qv\mu}{4\pi^2 \beta^2 n^2} K_0 \left(i \frac{\omega}{v} r \sqrt{\beta^2 n^2 - 1} \right) e^{-i \frac{\omega}{v} x}, \quad (37b)$$

with K_0 denoting the modified Bessel function of the second kind of order 0. From the definitions

$$\mathbf{H} = \frac{1}{\mu} \nabla \times \mathbf{A}, \quad (38a)$$

$$\mathbf{E} = -i\omega \mathbf{A} - \nabla \Phi, \quad (38b)$$

the solution (37) can be written in terms of the magnetic and electric fields as

$$\mathbf{H} = \begin{bmatrix} 0 \\ 0 \\ i \frac{q\omega}{4\pi^2 v} \sqrt{\beta^2 n^2 - 1} K_1 \left(i \frac{\omega}{v} r \sqrt{\beta^2 n^2 - 1} \right) e^{-i \frac{\omega}{v} x} \end{bmatrix}, \quad (39a)$$

$$\mathbf{E} = \begin{bmatrix} -i \frac{q\mu\omega}{4\pi^2 \beta^2 n^2} (\beta^2 n^2 - 1) K_0 \left(i \frac{\omega}{v} r \sqrt{\beta^2 n^2 - 1} \right) e^{-i \frac{\omega}{v} x} \\ i \frac{q\mu\omega}{4\pi^2 \beta^2 n^2} \sqrt{\beta^2 n^2 - 1} K_1 \left(i \frac{\omega}{v} r \sqrt{\beta^2 n^2 - 1} \right) e^{-i \frac{\omega}{v} x} \\ 0 \end{bmatrix}. \quad (39b)$$

The energy radiated through a cylindrical surface of radius R per unit travelled length x and per frequency ω can be computed as

$$\frac{d^2 W}{dx d\omega} = 4 \cdot 2\pi \cdot 2\pi R \cdot \Re(S_r), \quad (40)$$

with S_r being the radial component of the Poynting vector

$$\mathbf{S} = \frac{1}{2} \mathbf{E} \times \mathbf{H}^*. \quad (41)$$

It is worth pointing out that several pitfalls, arising for instance from the Fourier transform conventions and from the interval on which the energy density is defined (either $\omega \in (-\infty, \infty)$ or $\omega \in (0, \infty)$), may lead to incorrect multiplicative factors in the calculation of the Cherenkov radiation, compromising the accuracy of the results. A careful analysis on this topic can be found in [65] and the conventions adopted here are consistent with it. By substituting (39) in (40) and by replacing the modified Bessel function with the first term of its asymptotic expansion, the celebrated Frank–Tamm formula is derived

$$\frac{d^2 W}{dx d\omega} = \begin{cases} 0 & \text{for } \beta n \leq 1, \\ \frac{q^2 \mu}{4\pi} \omega \left(1 - \frac{1}{\beta^2 n^2} \right) & \text{for } \beta n > 1. \end{cases} \quad (42)$$

The results obtained with both the time- and the frequency-domain HDG solvers in Section 5.3 will be validated in terms of the shape of the Cherenkov cone, defined by the emission angle θ_C , and the emitted energy given by (42).

5. Numerical studies

5.1. Convergence of the methods

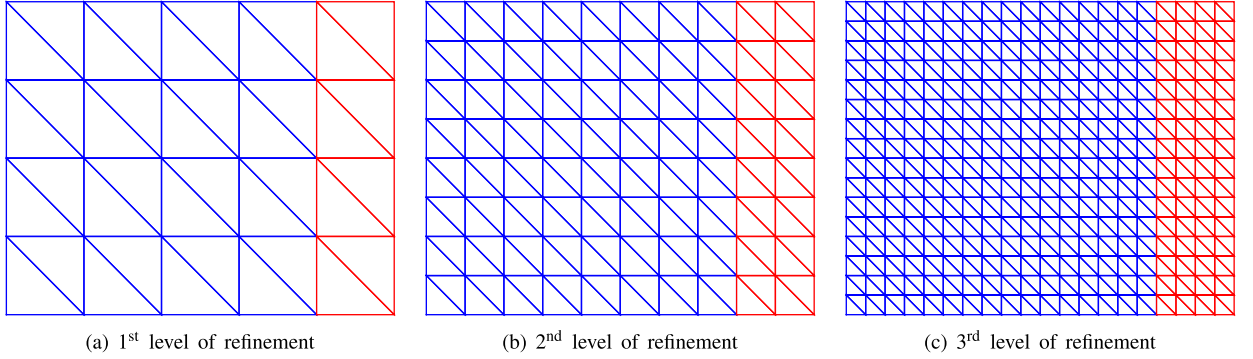


Fig. 2. Computational mesh for the wave propagation.

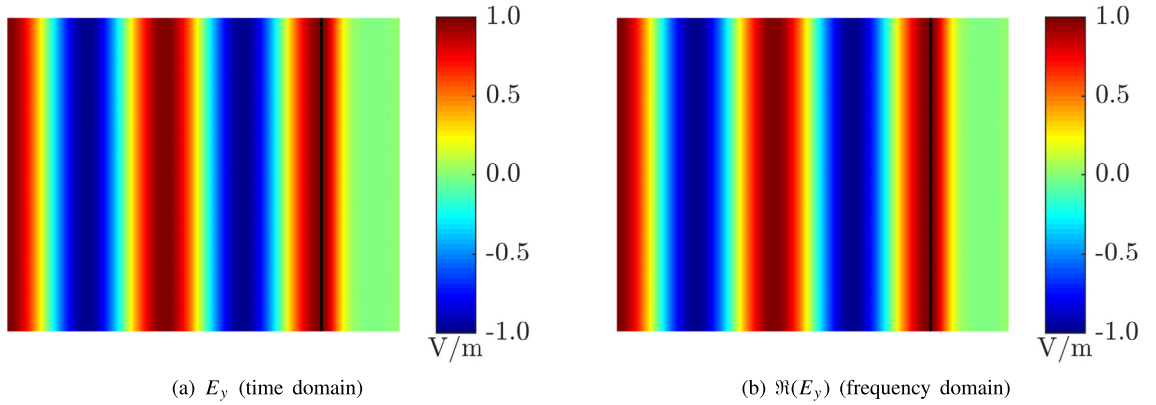


Fig. 3. Solution of the vertical electric field for the wave propagation.

The first numerical example considers the propagation of a plane wave in a uniform medium and its objective is to assess the convergence properties of the proposed HDG formulations for the solution of Maxwell's equations. To this end, two cases are considered in the following:

1. the problem is solved with the HDG formulation in the time domain according to Section 2,
2. the problem is solved with the HDG formulation in the frequency domain according to Section 3.

The electromagnetic wave is considered to be travelling along the x -direction and the corresponding magnetic and electric fields are given by

$$\begin{cases} H_z(x, y, t) = \sqrt{\varepsilon/\mu} \cos(\sqrt{\varepsilon\mu}\omega x - \omega t), \\ E_x(x, y, t) = 0, \\ E_y(x, y, t) = \cos(\sqrt{\varepsilon\mu}\omega x - \omega t), \end{cases} \quad (43)$$

in the time domain and by

$$\begin{cases} H_z(x, y, \omega) = \sqrt{\varepsilon/\mu} \cos(\sqrt{\varepsilon\mu}\omega x) - i\sqrt{\varepsilon/\mu} \sin(\sqrt{\varepsilon\mu}\omega x), \\ E_x(x, y, \omega) = 0, \\ E_y(x, y, \omega) = \cos(\sqrt{\varepsilon\mu}\omega x) - i \sin(\sqrt{\varepsilon\mu}\omega x), \end{cases} \quad (44)$$

in the frequency domain.

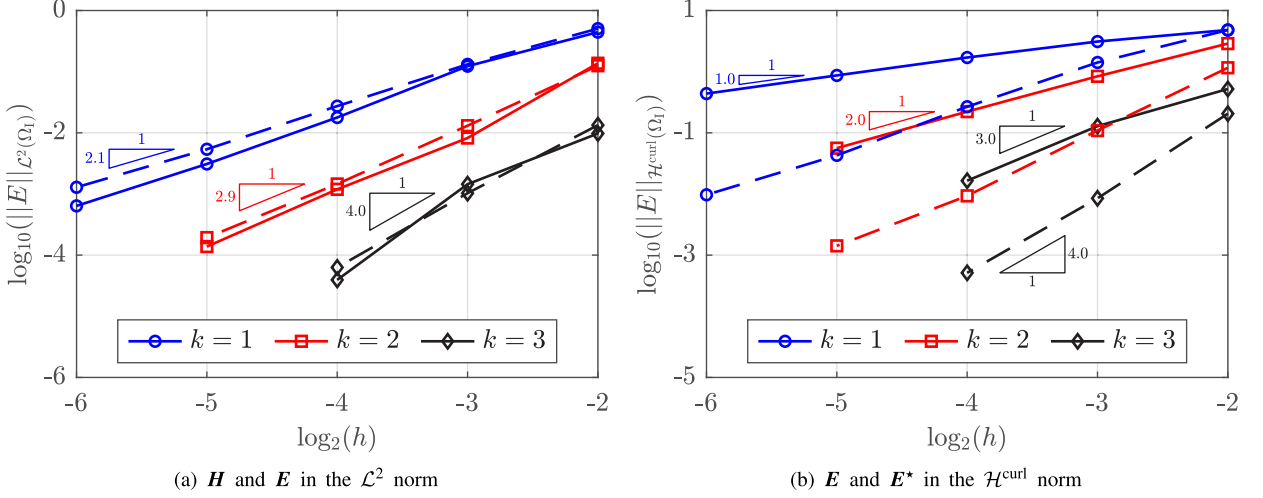


Fig. 4. Spatial convergence study of the time-domain solver.

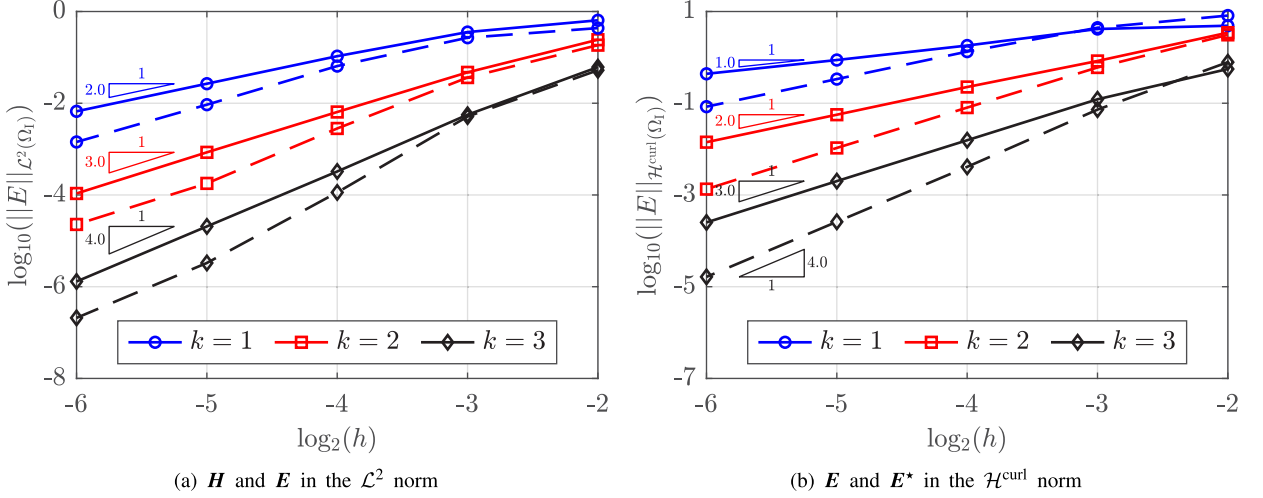


Fig. 5. Spatial convergence study of the frequency-domain solver.

The inner domain is the unit square $\Omega_I = (0, 1) \text{ m} \times (0, 1) \text{ m}$, whereas the PML region $\Omega_{\text{PML}} = (1, 1.25) \text{ m} \times (0, 1) \text{ m}$ is introduced to absorb the outgoing waves on the right side of the computational domain. Dirichlet boundary conditions, computed from the analytical solution, are imposed on the top, bottom and left sides of the domain, whereas absorbing conditions are used to terminate the PML region. The electromagnetic properties are set as $\varepsilon = 1 \text{ F/m}$ and $\mu = 1 \text{ H/m}$ and the angular frequency of the incoming wave is given by $\omega = 2\pi f$, with $f = 2 \text{ Hz}$. The stabilization parameters are considered constant on all faces and equal to $\tau_t = 1$ and $\tau_\omega = 10$ for the time-domain and the frequency-domain formulation, respectively. Only the damping function in the x -direction is adopted to absorb the wave within the PML region and it is evaluated according to (5), with $d_x = 0.25 \text{ m}$, $\bar{\sigma}_x = 100$ and $m = 1$. To perform the spatial convergence studies, uniform meshes are considered for the whole computational domain, by splitting a regular Cartesian grid into a total of $5 \cdot 2^{2l+1}$ triangles with characteristic element size $h = 1/2^{l+1} \text{ m}$. The first three levels of refinement, i.e. $l = [1, 2, 3]$, are shown in Fig. 2, where the blue and red colours refer to the discretization of the inner and the PML region, respectively. The polynomial degrees $k = [1, 2, 3]$ are considered for the approximation of all local and global unknowns. The resulting linear systems are solved with the direct UMFPACK (V5.4.0) solver both in the time and in the frequency domain.

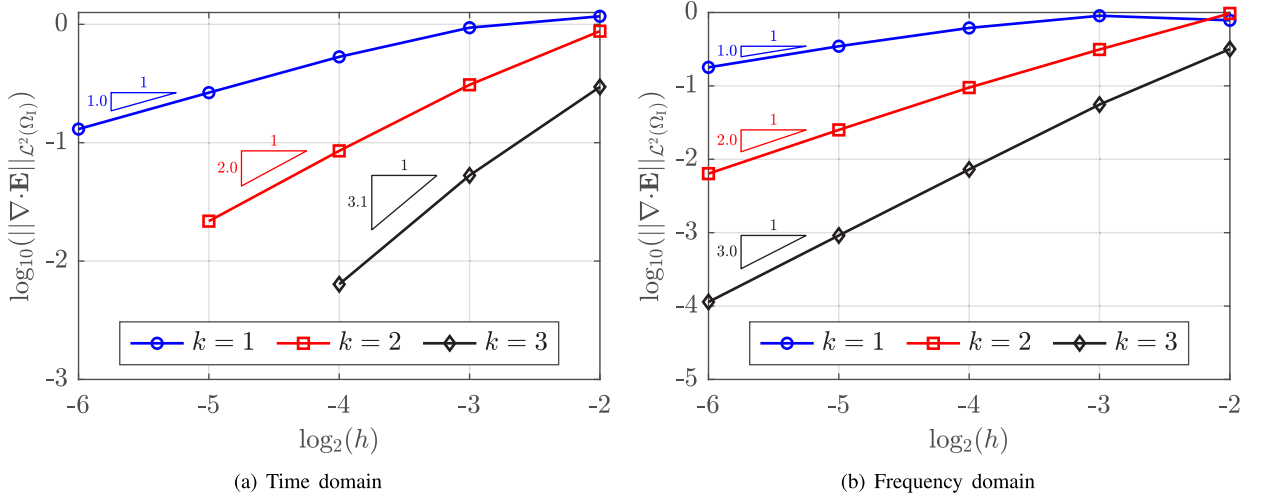


Fig. 6. Spatial convergence of the divergence of the electric field.

For the time-domain formulation, the primal and auxiliary electromagnetic fields are initialized at $t_i = 0$ s with homogeneous functions and the simulations are run until the final time $t_f = n_p \cdot 1$ s, with n_p denoting the number of periods, i.e. the number of times the wave travels the unit length. To eliminate the transient features, the number of periods considered are $n_p = [2, 8, 16]$ for $k = [1, 2, 3]$, respectively. Moreover, to keep the temporal error sufficiently smaller than the one produced by the spatial approximation, the evolution in time is carried out via the BDF2 scheme with time step sizes $\Delta t = [2^{-10}, 2^{-11}, 2^{-13}]$ s for $k = [1, 2, 3]$, respectively. The approximation of the vertical electric field obtained with $l = 3$ and $k = 3$ at the final time is shown on the left panel of Fig. 3. It is worth noting that the electromagnetic wave is properly absorbed in Ω_{PML} . As a result, the magnitude of the solution decreases rapidly from the maximum value 1 V/m at $x = 1$ m to 0 V/m at $x = 1.25$ m and no wave is reflected back in Ω_I . The convergence of the absolute error, evaluated at the final time according to (43) and computed over the inner domain, is plotted in Fig. 4 as a function of the characteristic element size h . More precisely, the left panel shows the error, measured in the L^2 norm, of the magnetic field \mathbf{H} (continuous lines) and the electric field \mathbf{E} (dashed lines). Both variables converge at the expected optimal rate, with order $k + 1$. The right panel compares instead the error in the $\mathcal{H}^{\text{curl}}$ norm of the electric field \mathbf{E} (continuous lines) and the postprocessed counterpart \mathbf{E}^* (dashed lines), computed through the strategy discussed in Section 2.6. It is clear that, while the primal field converges only with order k , the elemental problems (27) allow to construct an improved approximation of the electric field, superconverging in the $\mathcal{H}^{\text{curl}}$ norm with order $k + 1$.

As opposed to the time-domain formulation, the frequency-domain solver requires, at each mesh level l and polynomial degree k , the solution of only one global system for each frequency ω analysed. The real part of E_y , computed on $l = 3$ and $k = 3$, is shown on the right panel of Fig. 3. Similarly to the solution obtained with the time-domain solver, the electromagnetic wave is well absorbed within the PML region and no reflections are observed in the area of interest. The convergence results obtained by solving the problems (33), (34) and (35) are reported in Fig. 5. Although the error of the electric field is systematically smaller than the one of the magnetic field in the left panel, they both converge at the optimal rate of $k + 1$ in the L^2 norm. Finally, the right panel confirms the capability of the frequency-domain solver to produce a postprocessed electric field superconverging with order $k + 1$ in the $\mathcal{H}^{\text{curl}}$ norm, contrarily to the primal field converging with order k in the same norm.

As pointed out in Section 2.1, the proposed formulations do not enforce Gauss' laws explicitly. It is in fact well known that if the initial conditions satisfy Gauss' laws, then the solution will satisfy such laws for all times at the continuous level. However, this is not necessarily true at the discrete level. In fact, Gauss' laws for the electric and the magnetic field are satisfied in the numerical simulations only to discretization error. This is confirmed by the plots in Fig. 6, which show the convergence of the divergence of the electric field for both the time- (left panel) and the frequency- (right panel) domain formulations. It is clear that, since the electric field converges in the L^2 norm with order $k + 1$, its divergence converges with order k . The only non-zero component of the magnetic field is instead H_z , thus the divergence-free condition for the magnetic field is satisfied exactly by construction.

5.2. PML study

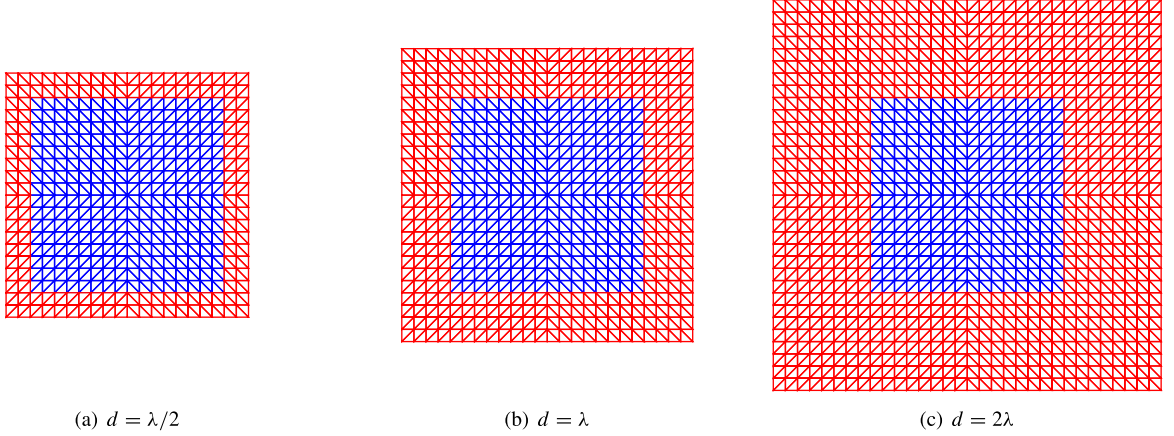


Fig. 7. Computational mesh for the PML study.

The second numerical example investigates the role of the thickness of the PML region and the polynomial scaling factor on the absorption of the electromagnetic field. The whole computational domain is defined as $\Omega = (-L - d, L + d) \times (-L - d, L + d)$, while the inner and the PML domains occupy the regions $\Omega_I = (-L, L) \times (-L, L)$ and $\Omega_{PML} = \Omega \setminus \Omega_I$, respectively. A unit edge length is considered for the inner domain, i.e. $L = 1$ m, whereas the thickness of the PML region d along the Cartesian coordinates is increased following a geometric progression. The parameter λ denotes the wavelength of the electromagnetic wave generated by the external current density

$$\begin{cases} j_x(x, y) = -\frac{1}{2\pi s^2} e^{-\frac{1}{2} \frac{x^2+y^2}{s^2}} \sin[\text{atan2}(y, x)], \\ j_y(x, y) = \frac{1}{2\pi s^2} e^{-\frac{1}{2} \frac{x^2+y^2}{s^2}} \cos[\text{atan2}(y, x)], \end{cases} \quad (45)$$

with $s = 1/16$ m being the standard deviation of the Gaussian distribution. The material parameters are taken as $\varepsilon = 1$ F/m and $\mu = 1$ H/m and the analysis is performed with the frequency-domain solver at the frequency $f = 2$ Hz, resulting in $\lambda = 1/2$ m.

A resolution of 16 nodes per wavelength is ensured by taking a constant element size $h = 1/8$ m with a quartic polynomial degree of approximation, i.e. $k = 4$. Absorbing boundary conditions are imposed on $\partial\Omega$. Following [67], for each d and m considered, the scaling parameter $\bar{\sigma}$ is varied as

$$\bar{\sigma} = \frac{m+1}{2d} \mathcal{R}. \quad (46)$$

The reflection error $e^{-\mathcal{R}}$ is set to be negligibly small by taking $\mathcal{R} = 20$. The thickness of the PML region is thus doubled at each successive simulation as $d = [\lambda/4, \lambda/2, \dots, 16\lambda]$ and four values are considered for the polynomial scaling factor, i.e. $m = [1, 2, 3, 4]$. The computational meshes corresponding to three different PML thicknesses are shown in Fig. 7.

The solution of the real part of the magnetic field in the z -direction, computed with $d = \lambda/2$ and $m = 2$, is exemplarily displayed on the left panel of Fig. 8. The magnetic field has the maximum at the origin of the reference system, it oscillates along the radial direction and it is absorbed in the PML region. The role of the PML thickness and the polynomial scaling factor on the absorption of the solution is analysed by monitoring the relative error of H_z at $(x, y) = (L/2, L/2)$, with the reference solution computed on the mesh corresponding to $d = 32\lambda$ and $m = 4$, counting more than 1 million global DOFs. The right panel of Fig. 8 clearly shows how the error decreases as d increases. Moreover, a higher m contributes to decreasing the error for $d \gtrsim \lambda/2$, but its effect remains small for $d \lesssim 2\lambda$. For very large ratios d/λ instead, the error decreases asymptotically with order $m + 1$.

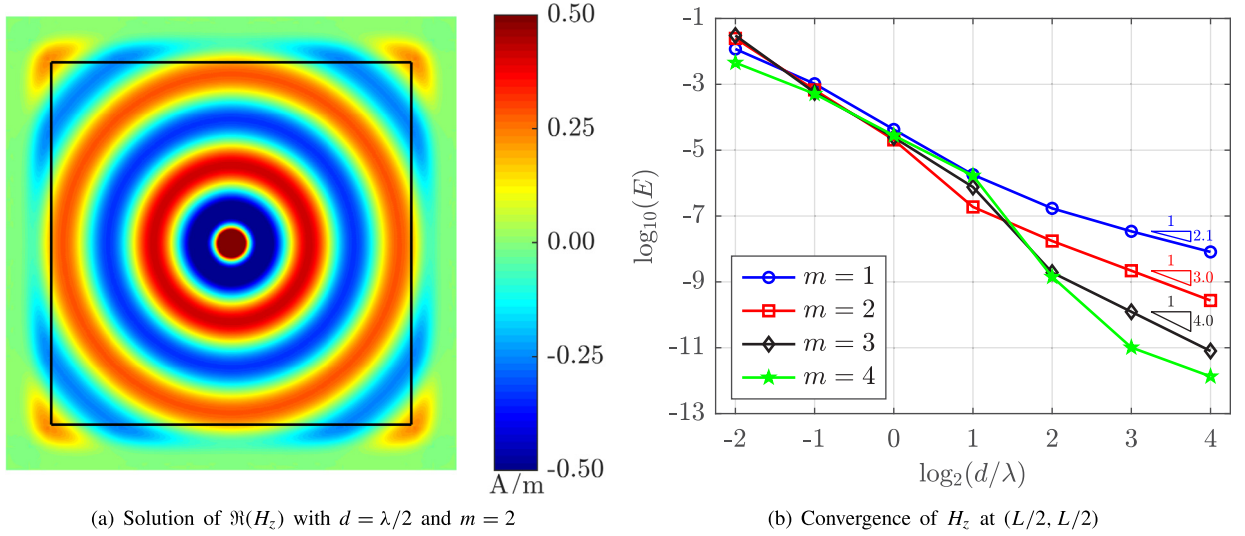


Fig. 8. Solution and convergence of the magnetic field for the PML study.

It is worth pointing out that a very large PML thickness would dramatically increase the number of unknowns. From a practical point of view, it is thus reasonable to select a moderate value of d/λ that provides a sufficient absorption of the electromagnetic field. In this numerical example, choosing $d = \lambda/2$ results in a relative error of less than 0.1%, regardless of m .

It is worth pointing out that, in principle, the PML thickness can be made arbitrarily thin by increasing $\bar{\sigma}$, thus making the exponential decay rate sufficiently rapid. However, as highlighted in [68], a very large scaling parameter can cause numerical reflections in the discretized problem. In such a case, a zero reflection can be recovered only for a vanishing mesh size, upon convergence to the continuum solution. With this regard, an hk -adaptive scheme, as the one adopted in [69], could represent a valid approach to minimize reflections to a desired level of accuracy, while retaining optimal computational efficiency.

5.3. Calculation of the Cherenkov radiation

The following set of numerical experiments aim at demonstrating the capability of the proposed solvers to accurately reproduce Cherenkovian effects on different scenarios.

The region of interest consists of a cylinder of length $L = 1$ m and radius $R = 0.5$ m. A charged particle travels along the x -axis at a velocity slightly lower than the speed of light in vacuum, i.e. $\beta = 0.9$. The domain is surrounded by a perfectly matched layer of thickness $d = 0.1$ m along the radial direction. A quadratic polynomial scaling factor, i.e. $m = 2$, is considered in Ω_{PML} , whereas the damping scaling parameter is set to $\bar{\sigma} = 100c_0$. The left and right faces of the cylinder are connected with periodic boundary conditions (Floquet-periodic when the frequency-domain solver is used), while the external boundary of the PML region is terminated with absorbing conditions. A sketch of the geometry and the boundary conditions is given in Fig. 9. The electrical parameters of free space are defined as $\mu_0 = 1.257 \cdot 10^{-6}$ H/m and $\varepsilon_0 = 8.854 \cdot 10^{-12}$ F/m, whereas the medium is characterized by its refractive index n . Three different materials are considered, i.e. air, water and glass, with refractive indices approximately equal to 1.00, 1.33 and 1.50, respectively.

First, the approach exposed in Section 2.5 is adopted to solve the Cherenkov problem in the 2D-axisymmetric components. The inner region is subdivided into 2^{2l+1} triangular elements, clustered along the x -axis, following a progression such that the ratio between the sizes of the elements adjacent to the PML region and of the elements adjacent to the x -axis is equal to 16. The PML region is then discretized with a uniform mesh which is conforming to the inner one and which contains an increasing number of elements along the thickness. Three different levels of mesh refinement are depicted in Fig. 10.

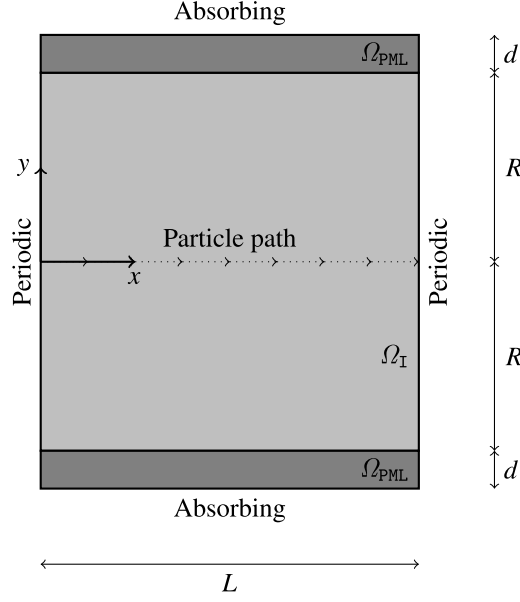


Fig. 9. Geometry and boundary conditions for the Cherenkov problem.

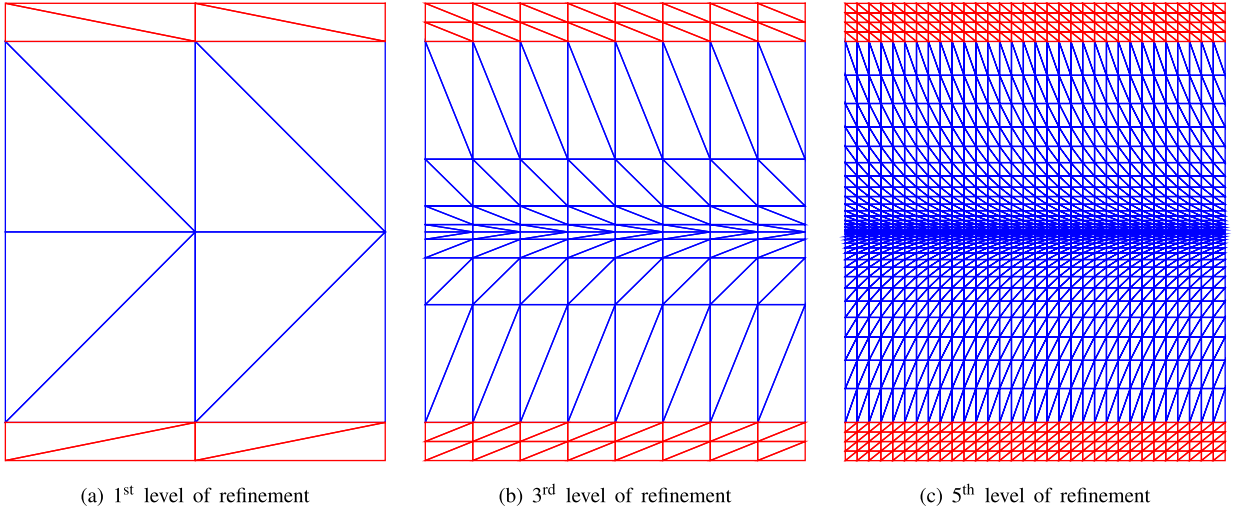


Fig. 10. Computational mesh for the 2D axisymmetric model.

The formulation in the time domain proposed in Section 2 is first considered. The effect of the fast-moving charge is analysed in the three different media (air, water and glass). The travelling charge is modelled by the current density (36) and by considering a unit charge. However, in the discrete setting, the Dirac delta functions in (36) are replaced by the smooth shape function

$$\psi(\eta) = \frac{15}{8\pi w^3} \left[1 - \left(\frac{\eta}{w} \right)^2 \right] \quad \text{for } \eta = 0, \dots, w, \quad (47)$$

with η denoting the distance from the centre of the particle and with w being the influence radius of the cloud. It is constructed as the generalization of the polynomial interpolation function “ S_{poll} ” (with a unit α) in [70] to

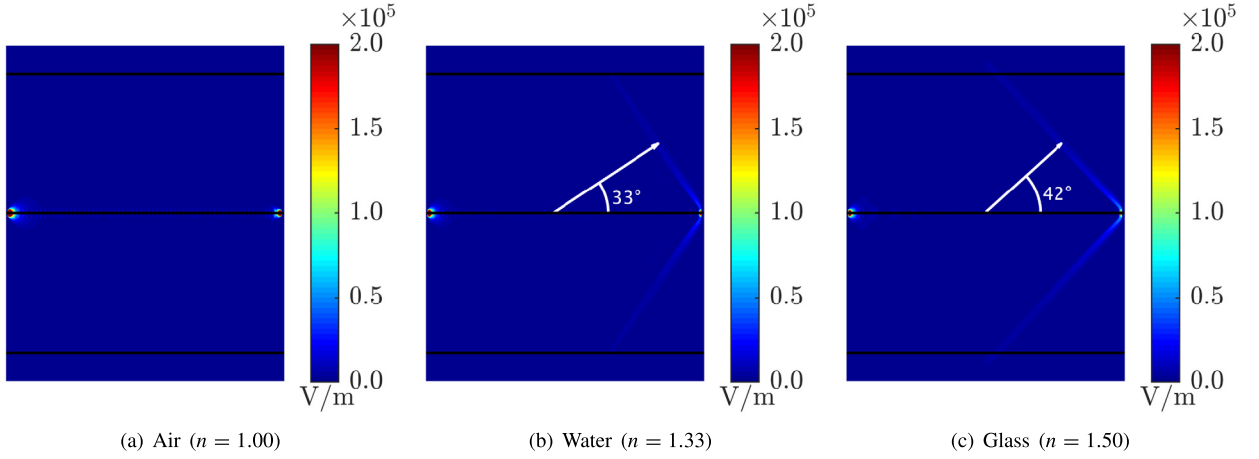


Fig. 11. Solution of the axial electric field in the time domain for different media with the 2D axisymmetric model.

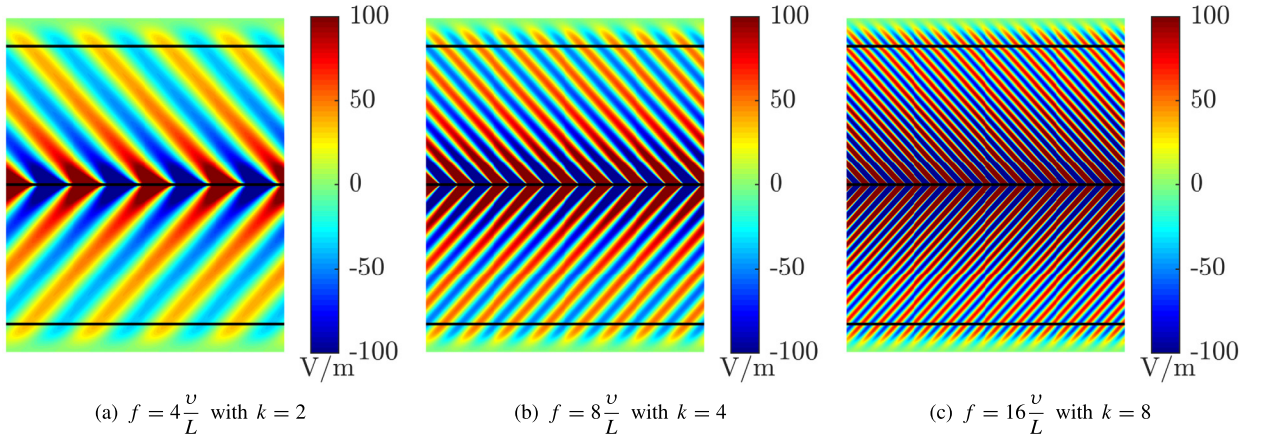


Fig. 12. Solution of the axial electric field in glass in the frequency domain for different frequencies with the 2D axisymmetric model.

the three-dimensional case. In particular, the multiplicative coefficient $15/(8\pi w^3)$ is obtained by requiring that $\int_0^{2\pi} \int_0^\pi \int_0^w \psi(\eta) \eta^2 \sin \varphi d\eta d\varphi d\theta = 1$. This type of shape function has been regarded in [70] as the least expensive to be evaluated, as opposed to alternative cosine and Gaussian distributions. The choice of w in (47) is important to properly simulate the travelling charge. On the one hand, large values would compromise the accurate representation of the point-like particle. On the other hand, however, excessively small values would yield noisy solutions [71]. In this work, it is chosen $w = \Delta x$, with Δx being the grid spacing along the x -direction.

Fig. 11 shows the final solution of the electric field in the axial direction, obtained with $l = 6$ and $k = 2$. The final time considered is $t_f = n_p L/v$ with $n_p = 8$ and the time step size is set as $\Delta t = 2^{-8} L/v$. In order to reproduce a periodic solution, the charged particle re-enters the computational domain at $x = 0$ m at the beginning of each period. This is achieved by defining $\eta = \sqrt{(x - \text{mod}(vt, L))^2 + y^2 + z^2}$, with mod denoting the modulo operator, i.e. the remainder after division of the travelled distance vt by the length L . From Fig. 11, it can be observed that no radiation is emitted in air, since the condition $\beta n > 1$ is not met. On the contrary, in water ($\beta n = 1.20$) and in glass ($\beta n = 1.35$) the travelling charge emits Cherenkov radiation at angles equal to $\theta_C = 33^\circ$ and 42° , respectively, which match the ones expected from theory. Moreover, by computing the discrete Fourier transform of the numerical solution over the last simulation period using the MATLAB implementation of the fast Fourier transform (based on [72]), by integrating the Poynting vector (41) over the surface of the cylinder and by dividing by its length, the radiated energy can be calculated. The values obtained at $f = 4v/L$ are $\frac{d^2 W}{dx d\omega} = 2.10 \cdot 10^2$ and $3.10 \cdot 10^2$ J-s/m

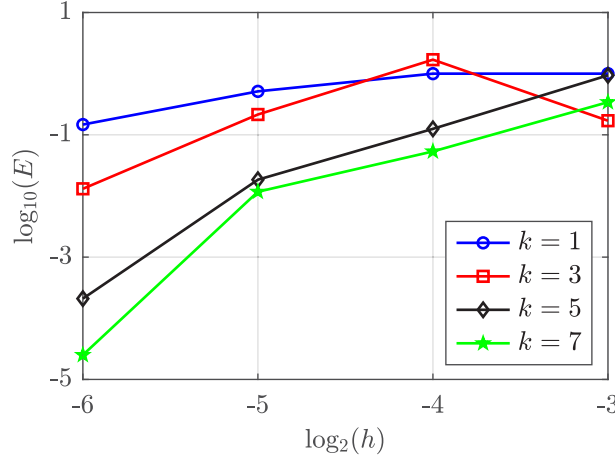


Fig. 13. Convergence of the Cherenkov radiation against the Frank–Tamm formula.

and they differ from the theoretical results given by the Frank–Tamm formula (42) by only 2.4% and 1.3% for water and glass, respectively. Writing the frequency as $f = n_f \nu / L$, with n_f being a scaling coefficient, provides a convenient way of selecting the frequency, independently of the particle velocity and the domain size considered. Clearly, if n_f is increased, a smaller time step size and a higher spatial resolution is needed to retain the same level of accuracy. This second aspect is analysed in more detail in the following frequency-domain simulations.

The capability of the frequency-domain formulation proposed in Section 3 to accurately simulate the Cherenkov radiation is then investigated. The effect of the travelling charge can be accounted for by the edge current [65]

$$I = \frac{q}{2\pi} e^{-i\frac{\omega}{v}x}. \quad (48)$$

For the present simulations, the axial current density has been set to

$$j_x(x, y, z, \omega) = \frac{1}{\pi w^2} \frac{q}{2\pi} e^{-i\frac{\omega}{v}x}, \quad (49)$$

within the first layer of elements adjacent to the x -axis, i.e. for $\sqrt{y^2 + z^2} \leq w$, with $w = \Delta r_1$ being the grid spacing along the radial direction for such layer of elements. The solution of the real part of the axial electric field $\Re(E_x)$ obtained in glass with the frequency-domain solver on $l = 6$ is shown in Fig. 12 for three different frequencies, i.e. $f = 4\nu/L$, $f = 8\nu/L$ and $f = 16\nu/L$. Given the increasing oscillatory nature of the solution with the frequency, the polynomial degree of approximation has been increased proportionally from $k = 2$ to $k = 8$. With this choice, the computed Cherenkov radiation differs from the theoretical one by less than 7% in all cases. If a linear polynomial approximation ($k = 1$) is used instead, the emitted radiation is underestimated by up to 64% for $f = 16\nu/L$. The capability of the HDG method to provide high-order approximations at a reasonable computational cost, owing to the hybridization of the elemental degrees of freedom (especially at high polynomial degrees, see for instance [73] in the context of flow problems), offers the flexibility to accurately study a wider range of frequencies by solely changing the polynomial degree, without the need of remeshing the computational domain. Moreover, by defining a desired level of accuracy and by interpreting the mismatch between the primal and the postprocessed solution as an error estimator, the polynomial adaptivity can be automatized as in [29–33].

To study the convergence of the emitted radiation towards the theoretical value given by (42), the relative error of the Cherenkov radiation at $f = 8\nu/L$ is plotted in Fig. 13 as a function of the characteristic element size h for $k = [1, 3, 5, 7]$. The computed radiation is severely underestimated for $k = 1$ and $h = 2^{-3}$ m, whereas its value progressively converges to the expected one for higher polynomial degrees and finer meshes. For $k = 7$ and $h = 2^{-6}$ m, the error reduces to $2.5 \cdot 10^{-5}$. It is worth pointing out that the error is not expected to achieve machine precision accuracy, since the Frank–Tamm formula (42) is obtained by approximating the modified Bessel function in (39) with its asymptotic expansion.

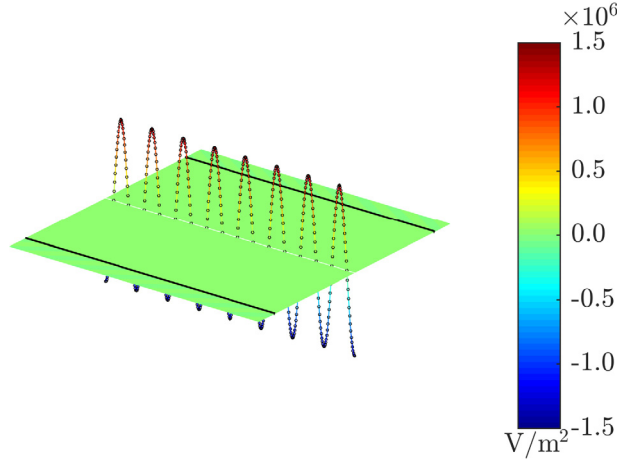


Fig. 14. Solution of the real part of the divergence of the electric field.

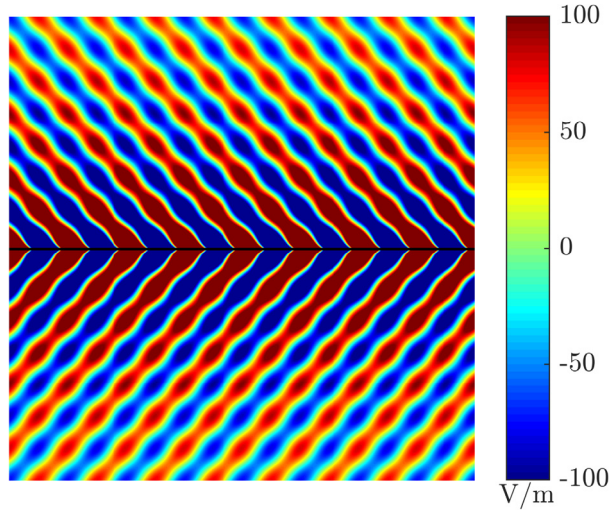


Fig. 15. Solution of the axial electric field in glass in the frequency domain with the 2D axisymmetric model without PML.

As in the example in Section 5.1, the satisfaction of Gauss's laws is analysed. The condition $\nabla \cdot \mathbf{B} = 0$ is satisfied exactly because $\mu = \text{const.}$ and the magnetic field has only the azimuthal component H_θ , which is invariant along θ , i.e. $\partial H_\theta / \partial \theta = 0$. Fig. 14 shows instead the real part of the divergence of the electric field at $f = 8\nu/L$ computed with $k = 7$ and $h = 2^{-6}$ m. Its value approaches zero in the inner computational domain, except within the first layer of elements adjacent to the axis in which the current density j_x is imposed. In this region the electric field should in fact satisfy the condition $\nabla \cdot \mathbf{E} = \rho/\epsilon$, with $\rho = j_x/\nu$. The black circles in Fig. 14 denote the analytical function ρ/ϵ , which matches closely the computed divergence of the electric field. Gauss' laws for the magnetic and the electric field can therefore be considered satisfied within discretization error.

The important role played by the perfectly matched layers for an effective absorption of the outgoing waves and an accurate computation of the Cherenkov radiation is evident by observing Fig. 15. It shows the axial electric field obtained at $f = 8\nu/L$ by replacing the PML region with absorbing boundary conditions. The irregular pattern of the solution is attributed to the partial reflection of the electromagnetic waves on the boundary of the computational domain. The relative error of the emitted radiation is as high as 48%, whereas the adoption of the proposed PML formulation on the same example reduces the error to less than 1%.

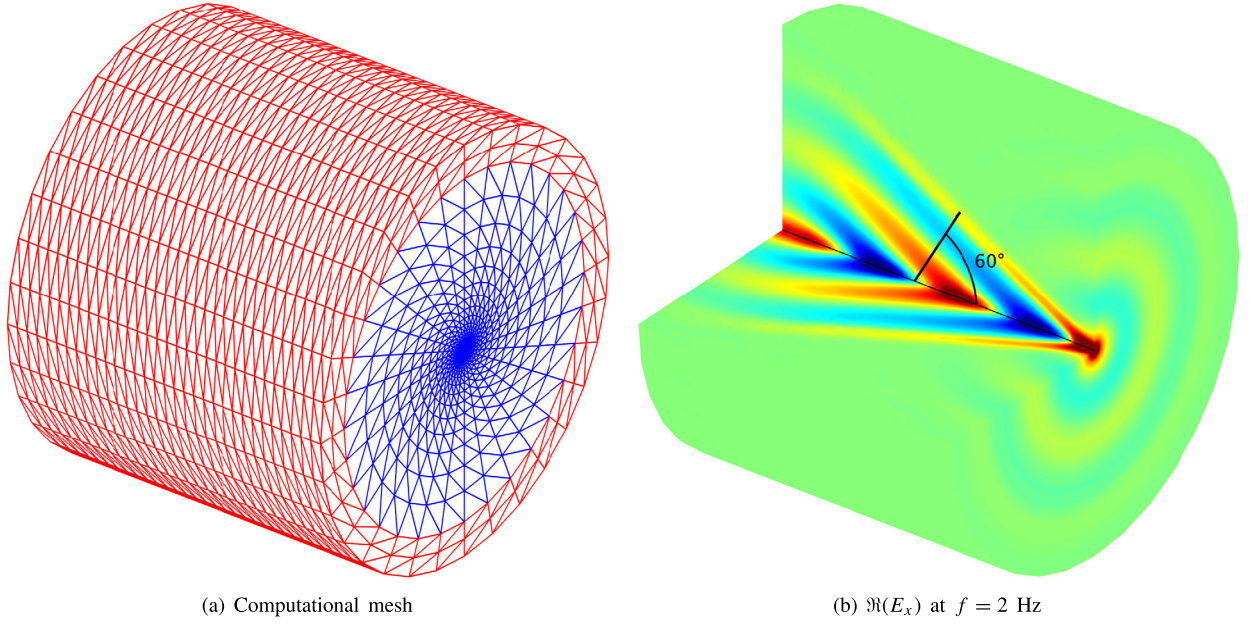


Fig. 16. Cherenkov problem with the 3D model.

In the following, the Cherenkov radiation is analysed in three dimensions. The meshes are constructed with GMSH [74] by extruding the two-dimensional meshes in Fig. 10 around the x -axis and subdividing the circumference into 2^l parts. Only two elements are considered along the thickness of the PML region. The resulting mesh on his fifth level of refinement counts 107 520 tetrahedral elements and it is shown on the left panel of Fig. 16. A quadratic polynomial degree of approximation is considered ($k = 2$), leading to a total number of 2 592 768 globally-coupled unknowns. A simplified set of parameters is considered, i.e. $\mu = 1$ H/m, $\beta = 1$ and $n = 2$. The problem is analysed in the time domain by considering one time period, i.e. $t_f = 1$ s, and a time step size of $\Delta t = 2^{-7}$ s. The resulting linear system is solved at each time step through a GMRES solver with relative tolerance of 10^{-3} and equipped with an ILU preconditioner. The solution is shown on the right panel of Fig. 16 in terms of the Fourier transform of the axial electric field. The emission angle is $\theta_C = 60^\circ$, as expected from theory. The Cherenkov radiation per unit travelled length computed at the frequency $f = 2$ Hz over a cylindrical surface of radius $1/8$ m is 0.71 J·s/m and differs from the one given by the Frank–Tamm formula by 5%, confirming the capability of the proposed approach to also solve three-dimensional problems.

6. Conclusion and future work

Two novel hybridizable discontinuous Galerkin formulations have been proposed to solve electromagnetic problems in the time and in the frequency domain. Special emphasis has been paid to the inclusion of perfectly matched layers, whose crucial role towards an accurate prediction of the emitted Cherenkov radiation has been shown in the numerical examples. The proposed approach requires minor changes in the local problems (that can be easily handled in parallel), but it does not alter the number of DOFs in the global system, consisting of the tangential component of the electric field on the mesh skeleton only. A strategy to solve axisymmetric problems by solely adding an extra term in the Ampere–Maxwell equation has been also discussed, together with the implementation aspects related to the inclusion of periodic boundary conditions in the time domain and Floquet-periodic conditions in the frequency domain in the HDG framework. A two-dimensional wave propagation problem has shown the capability of the proposed formulations to produce optimally convergent magnetic and electric fields in the \mathcal{L}^2 norm. Moreover, an inexpensive postprocessing procedure has been shown to produce an improved approximation of the electric field, converging with an additional order in the $\mathcal{H}^{\text{curl}}$ norm. A second numerical experiment has investigated the role of the thickness of the PML region and the polynomial scaling factor on the absorption of the electromagnetic field. A set of examples in 3D and 2D-axisymmetric components has then highlighted the

possibility to compute the Cherenkov radiation emitted by superluminal charged particles with a high level of accuracy. It could be of interest to include shock capturing strategies, developed mainly in the computational fluid dynamics community, to handle the strong gradients appearing in the solution of the Cherenkov problem in order to obtain sharp shock profiles while avoiding oscillations. Our future work will focus on embedding the proposed formulation into a multiphysics HDG framework to study the Cherenkov radiation emitted in soda-lime glass during hypervelocity impacts and to investigate the complex phenomena occurring in very short time scales.

Declaration of competing interest

The authors declare that they have no known competing financial interests or personal relationships that could have appeared to influence the work reported in this paper.

Acknowledgements

The support of ONR, United States of America grant N00014-21-1-2401 is gratefully acknowledged. We wish to thank Dr. Barsoum for his guidance throughout the project. We also express our gratitude to Dr. Berardocco for his useful suggestions to improve this paper.

References

- [1] J.D. Jackson, *Classical Electrodynamics*, John Wiley & Sons, 1999.
- [2] P.A. Cherenkov, Visible emission of clean liquids by action of γ radiation, *Proc. USSR Acad. Sci.* 2 (1934) 451.
- [3] A. Sasoh, *Compressible Fluid Dynamics and Shock Waves*, Springer, 2020.
- [4] J.V. Jelley, *Cherenkov Radiation and its Applications*, Pergamon Press, 1958.
- [5] Y.K. Akimov, Cherenkov detectors in particle physics, *Phys. At. Nucl.* 67 (7).
- [6] E. Branger, S. Grape, S.J. Svärd, P. Jansson, E.A. Sundén, On Cherenkov light production by irradiated nuclear fuel rods, *J. Instrum.* 12 (6) (2017) T06001.
- [7] E. Ciarrocchi, N. Belcari, Cherenkov luminescence imaging: physics principles and potential applications in biomedical sciences, *EJNMMI Phys.* 4 (1) (2017) 1–31.
- [8] S. Xi, H. Chen, T. Jiang, L. Ran, J. Huangfu, B.-I. Wu, J.A. Kong, M. Chen, Experimental verification of reversed cherenkov radiation in left-handed metamaterial, *Phys. Rev. Lett.* 103 (19) (2009) 194801.
- [9] D. Ziemkiewicz, S. Zielińska-Raczyńska, Cherenkov radiation combined with the complex Doppler effect in left-handed metamaterials, *J. Opt. Soc. Amer. B* 32 (8) (2015) 1637–1644.
- [10] Z. Duan, X. Tang, Z. Wang, Y. Zhang, X. Chen, M. Chen, Y. Gong, Observation of the reversed Cherenkov radiation, *Nature Commun.* 8 (1) (2017) 1–7.
- [11] H. Chen, M. Chen, Flipping photons backward: reversed Cherenkov radiation, *Mater. Today* 14 (1–2) (2011) 34–41.
- [12] R.G. Barsoum, Hypervelocity Impact of Soda Lime Glass Results in Cherenkov Radiation from Electromagnetic Plasma at Temperature Reaching 5700 Deg. K, Tech. rep., Office of Naval Research, 2020.
- [13] K. Yee, Numerical solution of initial boundary value problems involving Maxwell's equations in isotropic media, *IEEE Trans. Antennas and Propagation* 14 (3) (1966) 302–307.
- [14] P. Monk, *Finite Element Methods for Maxwell's Equations*, Oxford University Press, 2003.
- [15] D. Sun, J. Manges, X. Yuan, Z. Cendes, Spurious modes in finite-element methods, *IEEE Antennas Propag. Mag.* 37 (5) (1995) 12–24.
- [16] J.-C. Nédélec, Mixed finite elements in \mathbb{R}^3 , *Numer. Math.* 35 (3) (1980) 315–341.
- [17] J.-C. Nédélec, A new family of mixed finite elements in \mathbb{R}^3 , *Numer. Math.* 50 (1) (1986) 57–81.
- [18] A. Bossavit, A rationale for 'edge-elements' in 3-D fields computations, *IEEE Trans. Magn.* 24 (1) (1988) 74–79.
- [19] R.D. Graglia, D.R. Wilton, A.F. Peterson, Higher order interpolatory vector bases for computational electromagnetics, *IEEE Trans. Antennas and Propagation* 45 (3) (1997) 329–342.
- [20] J. Schöberl, S. Zaglmayr, High order Nédélec elements with local complete sequence properties, *COMPEL* (2005).
- [21] W.H. Reed, T.R. Hill, *Triangular Mesh Methods for the Neutron Transport Equation*, Tech. rep., Los Alamos National Laboratory, 1973.
- [22] I. Perugia, D. Schötzau, The hp-local discontinuous Galerkin method for low-frequency time-harmonic Maxwell equations, *Math. Comp.* 72 (2003) 1179–1214.
- [23] B. Cockburn, F. Li, C.-W. Shu, Locally divergence-free discontinuous Galerkin methods for the Maxwell equations, *J. Comput. Phys.* 194 (2) (2004) 588–610.
- [24] V. Dolean, H. Fahs, L. Fezoui, S. Lanteri, Locally implicit discontinuous Galerkin method for time domain electromagnetics, *J. Comput. Phys.* 229 (2) (2010) 512–526.
- [25] H. Fahs, S. Lanteri, A high-order non-conforming discontinuous Galerkin method for time-domain electromagnetics, *J. Comput. Appl. Math.* 234 (4) (2010) 1088–1096.
- [26] W.K. Anderson, L. Wang, S. Kapadia, C. Tanis, B. Hilbert, Petrov–Galerkin and discontinuous-Galerkin methods for time-domain and frequency-domain electromagnetic simulations, *J. Comput. Phys.* 230 (23) (2011) 8360–8385.

- [27] R. Sevilla, O. Hassan, K. Morgan, The use of hybrid meshes to improve the efficiency of a discontinuous Galerkin method for the solution of Maxwell's equations, *Comput. Struct.* 137 (2014) 2–13.
- [28] B. Cockburn, J. Gopalakrishnan, R. Lazarov, Unified hybridization of discontinuous Galerkin, mixed, and continuous Galerkin methods for second order elliptic problems, *SIAM J. Numer. Anal.* 47 (2) (2009) 1319–1365.
- [29] G. Giorgiani, S. Fernández-Méndez, A. Huerta, Hybridizable discontinuous Galerkin p-adaptivity for wave propagation problems, *Internat. J. Numer. Methods Fluids* 72 (12) (2013) 1244–1262.
- [30] G. Giorgiani, S. Fernández-Méndez, A. Huerta, Hybridizable discontinuous Galerkin with degree adaptivity for the incompressible Navier–Stokes equations, *Comput. & Fluids* 98 (2014) 196–208.
- [31] R. Sevilla, A. Huerta, HDG-NEFEM with degree adaptivity for Stokes flows, *J. Sci. Comput.* 77 (3) (2018) 1953–1980.
- [32] M. Giacomini, R. Sevilla, Discontinuous Galerkin approximations in computational mechanics: hybridization, exact geometry and degree adaptivity, *SN Appl. Sci.* 1 (9) (2019) 1047.
- [33] M. Giacomini, R. Sevilla, A. Huerta, HDGlab: an open-source implementation of the hybridisable discontinuous Galerkin method in MATLAB, *Arch. Comput. Methods Eng.* 28 (3) (2021) 1941–1986.
- [34] N.-C. Nguyen, J. Peraire, B. Cockburn, Hybridizable discontinuous galerkin methods for the time-harmonic Maxwell's equations, *J. Comput. Phys.* 230 (19) (2011) 7151–7175.
- [35] L. Li, S. Lanteri, R. Perrussel, A hybridizable discontinuous Galerkin method combined to a Schwarz algorithm for the solution of 3d time-harmonic Maxwell's equation, *J. Comput. Phys.* 256 (2014) 563–581.
- [36] A. Christophe, S. Descombes, S. Lanteri, An implicit hybridized discontinuous Galerkin method for the 3D time-domain Maxwell equations, *Appl. Math. Comput.* 319 (2018) 395–408.
- [37] L. Berardocco, M. Kronbichler, V. Gravemeier, A hybridizable discontinuous Galerkin method for electromagnetics with a view on subsurface applications, *Comput. Methods Appl. Mech. Engrg.* 366 (2020) 113071.
- [38] G.T. Di Francia, On the theory of some Čerenkovian effects, *Il Nuovo Cimento* 16 (1) (1960) 61–77.
- [39] I. Kaminer, S.E. Kooi, R. Shiloh, B. Zhen, Y. Shen, J.J. López, R. Remez, S.A. Skirlo, Y. Yang, J.D. Joannopoulos, A. Arie, M. Soljačić, Spectrally and spatially resolved Smith–Purcell radiation in plasmonic crystals with short-range disorder, *Phys. Rev. X* 7 (1) (2017) 011003.
- [40] R. Remez, N. Shapira, C. Roques-Carnes, R. Tirole, Y. Yang, Y. Lereah, M. Soljačić, I. Kaminer, A. Arie, Spectral and spatial shaping of Smith–Purcell radiation, *Phys. Rev. A* 96 (6) (2017) 061801.
- [41] A. Massuda, C. Roques-Carnes, Y. Yang, S.E. Kooi, Y. Yang, C. Murdia, K.K. Berggren, I. Kaminer, M. Soljačić, Smith–Purcell Radiation from low-energy electrons, *ACS Photonics* 5 (9) (2018) 3513–3518.
- [42] J. Zhou, Z. Duan, Y. Zhang, M. Hu, W. Liu, P. Zhang, S. Liu, Numerical investigation of Cherenkov radiations emitted by an electron beam bunch in isotropic double-negative metamaterials, *Nucl. Instrum. Methods Phys. Res. A* 654 (1) (2011) 475–480.
- [43] G. Burlak, Spectrum of Cherenkov radiation in dispersive metamaterials with negative refraction index, *Prog. Electromagn. Res.* 132 (2012) 149–158.
- [44] A.V. Tyukhtin, V.V. Vorobev, E.S. Belonogaya, S.N. Galyamin, Radiation of a charge in presence of a dielectric object: aperture method, *J. Instrum.* 13 (2) (2018) C02033.
- [45] S.N. Galyamin, A.V. Tyukhtin, V.V. Vorobev, Focusing the Cherenkov radiation using dielectric concentrator: simulations and comparison with theory, *J. Instrum.* 13 (2) (2018) C02029.
- [46] S.N. Galyamin, V.V. Vorobev, A. Benediktovitch, Radiation field of an ideal thin Gaussian bunch moving in a periodic conducting wire structure, *Phys. Rev. Accel. Beams* 22 (4) (2019) 043001.
- [47] K.-J. Bathe, H. Zhang, Y. Yan, The solution of Maxwell's equations in multiphysics, *Comput. Struct.* 132 (2014) 99–112.
- [48] D. Givoli, *Numerical Methods for Problems in Infinite Domains*, Elsevier, 2013.
- [49] J.-P. Berenger, A perfectly matched layer for the absorption of electromagnetic waves, *J. Comput. Phys.* 114 (2) (1994) 185–200.
- [50] R.W. Ziolkowski, Maxwellian material based absorbing boundary conditions, *Comput. Methods Appl. Mech. Engrg.* 169 (3–4) (1999) 237–262.
- [51] Y. Huang, J. Li, Numerical analysis of a PML model for time-dependent Maxwell's equations, *J. Comput. Appl. Math.* 235 (13) (2011) 3932–3942.
- [52] J. Li, J.S. Hesthaven, Analysis and application of the nodal discontinuous Galerkin method for wave propagation in metamaterials, *J. Comput. Phys.* 258 (2014) 915–930.
- [53] H. Barucq, F. Delaunay, B. Hanouzet, Method of absorbing boundary conditions: phenomena of error stabilization, *SIAM J. Numer. Anal.* 35 (3) (1998) 1113–1129.
- [54] J.-M. Jin, W.C. Chew, Combining PML and ABC for the finite-element analysis of scattering problems, *Microw. Opt. Technol. Lett.* 12 (4) (1996) 192–197.
- [55] H.K. Chaurasia, N.-C. Nguyen, J. Peraire, A time-spectral hybridizable discontinuous Galerkin method for periodic flow problems, in: 21st AIAA Computational Fluid Dynamics Conference, 2013.
- [56] C. Ciucă, P. Fernandez, A. Christophe, N.-C. Nguyen, J. Peraire, Implicit hybridized discontinuous Galerkin methods for compressible magnetohydrodynamics, *J. Comput. Phys.: X* 5 (2020) 100042.
- [57] L. Berardocco, Hybridizable Discontinuous Galerkin Methods for time-domain electromagnetic diffusion in conductive media (Ph.D. thesis), Technische Universität München, 2021.
- [58] A. La Spina, J. Fish, A superconvergent hybridizable discontinuous Galerkin method for weakly compressible magnetohydrodynamics, *Comput. Methods Appl. Mech. Engrg.* 388 (2022) 114278.
- [59] A. Montlaur, S. Fernández-Méndez, A. Huerta, Discontinuous Galerkin methods for the Stokes equations using divergence-free approximations, *Internat. J. Numer. Methods Fluids* 57 (9) (2008) 1071–1092.

- [60] B. Cockburn, B. Dong, J. Guzmán, A superconvergent LDG-hybridizable Galerkin method for second-order elliptic problems, *Math. Comp.* 77 (264) (2008) 1887–1916.
- [61] B. Cockburn, N.-C. Nguyen, J. Peraire, A comparison of HDG methods for Stokes flow, *J. Sci. Comput.* 45 (1) (2010) 215–237.
- [62] N.-C. Nguyen, J. Peraire, B. Cockburn, An implicit high-order hybridizable discontinuous Galerkin method for linear convection–diffusion equations, *J. Comput. Phys.* 228 (9) (2009) 3232–3254.
- [63] N.-C. Nguyen, J. Peraire, B. Cockburn, An implicit high-order hybridizable discontinuous Galerkin method for nonlinear convection–diffusion equations, *J. Comput. Phys.* 228 (23) (2009) 8841–8855.
- [64] N.-C. Nguyen, J. Peraire, B. Cockburn, An implicit high-order hybridizable discontinuous Galerkin method for the incompressible Navier–Stokes equations, *J. Comput. Phys.* 230 (4) (2011) 1147–1170.
- [65] A. Szczepkiewicz, L. Schächter, R.J. England, Frequency-domain calculation of Smith–Purcell radiation for metallic and dielectric gratings, *Appl. Opt.* 59 (35) (2020) 11146–11155.
- [66] L. Schächter, *Beam-Wave Interaction in Periodic and Quasi-Periodic Structures*, Springer Science & Business Media, 2013.
- [67] A. Taflové, *Computational Electrodynamics: The Finite-Difference Time-Domain Method*, Artech House, 1995.
- [68] S.G. Johnson, Notes on perfectly matched layers (PMLs), arXiv:2108.05348.
- [69] C. Michler, L. Demkowicz, J. Kurtz, D. Pardo, Improving the performance of perfectly matched layers by means of hp-adaptivity, *Numer. Methods Partial Differential Equations* 23 (4) (2007) 832–858.
- [70] G.B. Jacobs, J.S. Hesthaven, High-order nodal discontinuous Galerkin particle-in-cell method on unstructured grids, *J. Comput. Phys.* 214 (1) (2006) 96–121.
- [71] A.C. Fletcher, S. Close, Particle-in-cell simulations of an RF emission mechanism associated with hypervelocity impact plasmas, *Phys. Plasmas* 24 (5) (2017) 053102.
- [72] M. Frigo, S.G. Johnson, FFTW: An adaptive software architecture for the FFT, in: *Proceedings of the 1998 IEEE International Conference on Acoustics, Speech and Signal Processing*, Vol. 3, 1998, pp. 1381–1384.
- [73] M. Paipuri, S. Fernández-Méndez, C. Tiago, Comparison of high-order continuous and hybridizable discontinuous Galerkin methods for incompressible fluid flow problems, *Math. Comput. Simulation* 153 (2018) 35–58.
- [74] C. Geuzaine, J.-F. Remacle, Gmsh: A 3-D finite element mesh generator with built-in pre-and post-processing facilities, *Internat. J. Numer. Methods Engrg.* 79 (11) (2009) 1309–1331.